# IMAGE PROCESSING ALGORITHMS FOR HISTOPATHOLOGICAL IMAGES

A THESIS SUBMITTED TO
THE GRADUATE SCHOOL OF ENGINEERING AND SCIENCE
OF BILKENT UNIVERSITY
IN PARTIAL FULFILLMENT OF THE REQUIREMENTS FOR
THE DEGREE OF
MASTER OF SCIENCE
IN
ELECTRICAL AND ELECTRONICS ENGINEERING

By
Oğuzhan Oğuz
March 2016

Image Processing Algorithms for Histopathological Images
By Oğuzhan Oğuz
March 2016

We certify that we have read this thesis and that in our opinion it is fully adequate, in scope and in quality, as a thesis for the degree of Master of Science.

Ahmet Enis Çetin(Advisor)

Serdar Kozat

Kasım Taşdemir

Approved for the Graduate School of Engineering and Science:

Levent Onural
Director of the Graduate School

# ABSTRACT

# IMAGE PROCESSING ALGORITHMS FOR HISTOPATHOLOGICAL IMAGES

Oğuzhan Oğuz
M.S. in Electrical and Electronics Engineering
Advisor: Ahmet Enis Çetin
March 2016

Conventionally, a pathologist examines cancer cell morphologies under microscope. This process takes a lot of time and is subject to human mistakes. Computer aided diagnosis (CAD) systems and modules aim to help pathologists in their work to decrease the time consumption and the human mistakes. This thesis proposes a CAD module and algorithms which assist the pathologist in segmentation, detection and the classification problems in histopatholgic images. A multi-resolution super-pixel based segmentation algorithm is developed to measure the cell size, count the number of cells and track the motion of cells in Mesenchymal Stem Cell (MSC) images. The proposed algorithm is compared with Simple Linear Iterative Clustering (SLIC) algorithm. It is experimentally observed that in the segmentation stage, the cell detection rate is increased by 7% and the false alarm is decreased by 5%. In addition to this, two novel decision rules for merging similar neighboring super-pixels are proposed. One dimensional version of the Scale Invariant Feature Transform (SIFT) based merging algorithm is developed and applied to the histograms of the neighboring super-pixels to determine the similar regions. It is also shown that the merging process can be made with the use of wavelets. Moreover, it is shown that region covariance and codifference matrices can be used in detection of cancer stem cells (CSC) and a CAD module for the CSC detection in liver cancer tissue images are developed. The system locates CSCs in CD13 stained liver tissue images. The method has an online learning approach which improves the accuracy of detection. It is experimentally shown that, applying the proposed approach with the user guidance,increases the overall detection quality and accuracy up to 25% compared to using region descriptors alone. Also, the proposed module is compared with the similar plug-ins of ImageJ and Fiji. It is shown that, when the similar features are used, the implemented module achieves approximately 20% better classification

results compared to the plug-ins of Imagej and Fiji. Furthermore, the proposed 1-D SIFT algorithm is expanded and used in classification of the cancer tissues images stained with Hematoxylin and Eosin (H&E) stain, which is a cost effective routine compared to the immunohistochemistry (IHC) procedure. The 1-D SIFT algorithm is able to classify healthy and cancerous tissue images with up to 91% accuracy in H&E stained images in our data set.

*Keywords:* Super-Pixel, 1-D SIFT, Wavelet Transform, Region Covariance Matrix, Region Co-difference Matrix, Cancer Stem Cells, CD13 Stain, H&E Stain.

# ÖZET

# HİSTOPATOLOJİK İMGELER İÇİN İMGE İŞLEME ALGORİTMALARI

Oğuzhan Oğuz
Elektrik ve Elektronik Mühendisliği, Yüksek Lisans
Tez Danışmanı: Ahmet Enis Çetin
Mart 2016

Pataloglar hücre morfolojilerini mikroskop altında incelemektedirler. Bu işlem zaman almasının yanı sıra insan kaynaklı hatalara da açıktır. Bilgisayar tabanlı tanı sistemleri ve modülleri, pataloglara bu ağır işte yardımcı olarak harcanan zamanı ve insan kaynaklı hataları azaltmaktadır. Bu tezde, histopatholojik imgelerdeki bölütleme, saptama ve ayrıştırma sorunlarında pataloglara yardm etmek amacıyla bilgisayar tabanlı bir tanı mödülü ve algoritmalar geliştirilmiştir. Mezenkimal kök hücrelerinin (MKH) boyutunun ölçülmesi, sayımı ve hareketlerinin takip edilmesi amacıyla çok çözünürlüklü süper piksel algoritması sunulmuştur. Sunulan bu algoritma, Basit Doğrusal Dönüşümlü Gruplandırma (SLIC) algoritması ile karşılaştırılmış ve hücrelerin bulunmasında %7 oranında bir atış yakalanırken, %5 daha az yanlış alarm oranı elde edilmiştir. Ayrıca benzer komşu süper pikselleri birleştiren özgün iki yeni karar verme algoritmaları sunulmuştur. Skaladan Bağımsız Özellik Transformunun (SIFT) tek boyutaki versiyonu geliştirilmiş ve benzer bölgelerin bulunması amacıyla komşu süper piksellerin histogramlarına uygulanmıştır. Aynı birleştirme işleminin dalgacık teoremi kullanılarak da yapılabilineceği gösterilmiştir. Bahsedilenlere ek olarak, kovaryans ve ortak fark matrikslerinin kanser kök hücrelerinin (KKH) bulunmasında kullanılabilineceği gösterilmiş ve karaciğer imgelerindeki aynı hücrelerin sezimlenmesi için bir bilgisayar tabanlı tanı modülü geliştirilmiştir. Geliştirilen algoritma, CD13 boyaması ile boyanmış karaciğer kanseri imgelerdeki kanser kök hücrelerini bulmaktadır. Sistemin gerçek zamanlı öğrenmeye açık yapısı ile saptama başarısı arttırılmıştır. Sunulan algoritma kullanıcı yönlendirmesi ile çalıştığında, sadece bölge tanımlayıcıları kullanılarak elde edilen sonuçlara nazaran ortalama bulma kalitesinin ve doğruluğun 25% oranında yükseldiği deneysel olarak gösterilmiştir. Ayrıca, sunulan bu modül, ImageJ ve Fiji programlarının yakın eklentileri ile karşılaştırılmış ve benzer öznitelikler kullanıldığında, sunulan modülü ile,

eklentilere göre yaklaşık %20 daha başarılı ayrıştırma sonuçları elde edildiği gösterilmiştir. Sunulan sistem ile beraber daha önce bahsedilen tek boyutlu SIFT algoritması geliştirilerek immünohistokimyasal prosedürlere göre masrafsız bir boyama olan Hematoksilen-Eozin (H&E) boyaması ile boyanmış kanserli imgelerin ayrıştırılmasında kullanılmıştır. Önerilen yöntem ile H&E boyaması uygulanmış normal ve kanserli dokuların ayrıştırılmasında %91 gibi bir başarı yüzdesi elde edilmiştir.

*Anahtar sözcükler*: Süper Piksel, 1-D SIFT, Dalgacık Dönüşümü, Bölge Kovaryans Matrisi, Bölge Ortak Fark Matrisi, Kanser Kök Hücreleri, CD13 Boyaması, H&E Boyaması..

# Acknowledgement

First of all, I would especially like to thank Prof. Dr. A. Enis Çetin for giving me a chance to have M.Sc. degree in Bilkent University. Without his guidance and suggestions I would not be able to improve myself in such a great way.

Special thanks to Assoc. Prof. Serdar Kozat and Asst. Prof. Kasım Taşdemir for reading and making suggestions on this thesis.

I would like to thank Prof. Rengül Çetin Atalay and Prof. İhsan Sabuncuoğlu for their guidance and support.

My gratitude to my friends Onur Yorulmaz, Onur Külçe, Osman Günay, Ece Akhan, Deniz Yıldırım, Maen Mallah, Sinan Alemdar, Muhammed Tofighi, Damla Sarca, Ecem Bozkurt, İpek Hüyüklü, Gizem Tezyürek, İdil Kanpoat, Sinem Sav and all my colleagues in EE310 for their help, friendship and time.

I would also like to thank to Mürüvet Parlakay, Ebru Ateş, Görkem Uğuroğlu for their efforts and coffees.

Special thanks to TÜBİTAK for supporting this work under Grant Numbers 113E069 and 213E032.

I would like to thank my friends Sena Erdemir, Devrim Şahin and Tunç Arslan and for sharing valuable moments of my life and laughters.

Finally my thanks to Lara Eral for supporting me with her love and friendship.

It is a pleasure to express my thanks to all my family. Especially to my mother, father and brother for their endless love and support.

# Contents

# List of Figures

# List of Tables

# Chapter 1

# Introduction

Cancer is considered to be one of the most lethal diseases in the world. According to the World Cancer Report published by the International Agency for Research on Cancer in 2014 [1], approximately 14 million people experience this disease every year and almost 8 million people have died of it. As a term, "cancer" is a common name for malignant tumors. These tumors grow rapidly and abnormally. Then they spread to different organs and tissues. This invasion is called metastatic invasion. It is important to observe the level of metastasis in a tissue because the metastasis itself is one of the major reasons of the deaths.

A pathologist can grade the level of metastasis under a microscope with the help of certain tissue stains. He or she first takes tissue samples from the patient and then slices thin layers from the sample. Staining the layers before investigating under the microscope helps to highlight the related parts and makes the cancerous cell distinguishable. Hematoxylin and Eosin (H&E) staining is a commonly used procedure to this end. It is possible to observe cancer cells in a tissue stained with H&E staining. In order to increase the reliability, computer based algorithms are also developed for this purpose. Many studies have been conducted with H&E stain. In [2], H&E stained prostate cancer images are segmented and morphological features of the segmented areas are extracted. The classification process is done with the use of random Markov fields. In [3], H&E

stained breast cancer tissues are used as a data set. After extracting graph based architectural features such as Voronoid diagram [4], Delanuay triangulation [5], minimum spanning tree [6] etc., they perform classification using Support Vector Machines (SVM). It is also important to detect the cancer stem cells (CSC) in a tissue because these cells stimulate the reproduction of the malignant tumors. More detailed information about histopathologic image analysis can be found in [7]. However, it is not possible to observe the CSCs in H&E stained images. The CD13 stain is one of the markers used for visualizing CSCs. For a pathologist it is perceptually easier to detect the CSCs in microscopic images of the tissues stained with CD13 antibodies by immunohistochemstry. On the other hand, staining with CD13 antibodies is costly compared to the prevalent Hematoxylin and Eosin (H&E) staining.

In contrast to the devastating effects of cancer stem cells and malignant tumors, Mesenchymal Stem Cells (MSC) are used for healing purposes. In the case of tissue injury, these cells travel to the damaged site and help tissue to heal without causing a reaction in the immune system. MSCs are commonly used in cellular therapies. These cells are visualized with the use of fluorescent microscope. The fluorescent microscope is generally used to examine examples using re-radiation occurrence of fluorescence [8–11].

As mentioned, cancer tissue grading, cancer stem cell information, analysis of metastatic invasion, detection and tracking mesenchymal stem cells etc. can be acquired from the microscopic images with the help of a pathologist. Recently developed computer assisted digital pathology systems can help pathologists in these time consuming processes. By using a proper computer-aided diagnosis (CAD) system and modules, not only the diagnosis time but also human based errors can be significantly reduced. There are some commercial and non-commercial CAD system packages which aim to facilitate the use of different CAD modules in one software. ImageJ [12] is a Java based open source application which enables users to perform various biomedical image processing procedures. Fiji [13], which is an advanced version of ImageJ, combines the different plug-in libraries of ImageJ. Cell Profiler [14] is a MATLAB® based CAD system. It is useful for cell counting, cell shape and texture analysis, revealing cell pathways targeted by different

drugs. As an important open source environment Open Microscopy Environment (OME) [15, 16] and its image data management tool OMERO [17] aim to standardize image information, extraction and transfer. Although it does not directly aim to serve as a CAD system with its plug-ins like WND-CHARM [18], many image processing applications can be performed. Detailed information about other CAD systems such as V3D, Icy and KNIME can be found in [19–21]. More detailed information about CAD systems and modules can be found in [11].

This thesis proposes a CAD module and algorithms for classification, segmentation, and detection of both mesenchymal and cancer stem cells in certain histopathological images. The outline of the thesis is as follows: In Chapter 2, a new super-pixel algorithm is proposed to segment MSC in fluorescent microscopy images with varying super-pixel sizes. Also, a Scale Invariant Feature Transform (SIFT) [22] and wavelet based merging methods are proposed to merge similar neighboring super-pixels. In Chapter 3, a CAD system for CSC detection in CD13 stained liver tissue images are developed. It is shown that CSCs in CD13 stained tissue images can be automatically identified using region covariance and co-difference descriptors [23–25]. Later, CSCs in CD13 stained liver tissue images are located using an online learning algorithm by combining several learners. Initially, this algorithm linearly combines region covariance, co-difference and color descriptors. Based on the feedback from a pathologist, the algorithm updates the weights of individual descriptors. This weight update strategy is similar to the least mean square (LMS) based online decision fusion strategy used in some other image and video processing problems [26, 27]. In Chapter 3, a texture analysis based image classification algorithm is proposed for H&E stained images of liver tissues. The algorithm analyzes H&E images using one-dimensional Scale Invariant Feature Transform (1-D SIFT) features. Conclusions and contributions are given in Chapter 4.

# Chapter 2

# Applications on Fluorescent Mesenchymal Stem Cells Images

The aim of the super-pixel algorithms is to divide images into small groups of similar pixels for further high level processing. Super-pixels are used for object tracking [28], body pose estimation [29] and three-dimensional (3D) applications [30].

Super-pixel algorithms start by dividing the image into uniform segments. Iterative algorithms are used to modify the uniform segments into regions that try to cover similar pixels. Similarity measures include a combination of pixel distance in coordinates and color distance in various color spaces. In some implementations the contribution of each distance measure has normalized weights. In [31], the weights are updated adaptively. Depending on the aim, different color spaces such as L,a,b [31] or ordinary red, green, blue (r,g,b) are used.

## 2.1 Multi-resolution Super-Pixels

The multi-resolution super-pixel algorithm can be based on any other super-pixel method. In this thesis, Simple Linear Iterative Clustering (SLIC) [31] method is used as the underlying super-pixel method. In a typical super-pixel method, initial seed positions are uniformly placed throughout the image. As a result, initial super-pixel regions have honeycomb shapes. On the other hand, the proposed algorithm starts with a non-uniform distribution of seed locations, which are determined according to the local wavelet domain energy of the image. Around the edges the wavelet energy representing high frequency activity is higher than smooth areas. Therefore, it is expected to have more super-pixels in high-frequency regions of a given image.

Let $x[n_1, n_2]$ be a 2-D microscopic image. It is processed by a wavelet high-pass filter both vertically and horizontally. Let $y_h[n_1, n_2]$ be the horizontally filtered image, which is obtained as:

$$y_h[n_1, n_2] = \sum_{l=0}^{L-1} x[l - n_1, n_2] * h[l] \quad , \tag{2.1}$$

where $h[l]$ is a half-band wavelet high-pass filter (HPF) with length $L$. The impulse response of the HPF is $h[l] = (-\frac{1}{4}, \frac{1}{2}, -\frac{1}{4})$. In a similar manner, $y_v[n_1, n_2]$ is obtained by vertical filtering as:

$$y_v[n_1, n_2] = \sum_{l=0}^{L-1} x[n_1, l - n_2] * h[l] \quad . \tag{2.2}$$

Both $y_h$ and $y_v$ contain undecimated wavelet coefficients. This process is applied to all three color channels of the image. An image $y_e$, representing the edge information of the original image $x$ is obtained by:

$$y_e = |y_{h,r}| + |y_{h,g}| + |y_{h,b}| + |y_{v,r}| + |y_{v,g}| + |y_{v,b}| \quad , \tag{2.3}$$

where the subscripts $r$, $g$, and $b$ represent red, green and blue channels respectively, and $h$ and $v$ represent horizontal and vertical high-pass filtering respectively.

Uniform placement of initial seeds in ordinary super-pixel algorithms leads to honeycomb shaped super-pixels regions on the image. In the proposed approach, additional seeds are placed between two connected seeds when a region between them has high wavelet energy values. To do this, two positions on the connecting line between the two seed locations are checked for their high frequency content. The two positions correspond to 1/4th and 3/4th of the length of each connecting line. A threshold is applied to $y_e[n_1, n_2]$ components to decide whether to place a new seed in the midpoint of two connected seeds. This threshold is calculated as:

$$t = \frac{1}{4}(max(y_e[n_1, n_2]) + min(y_e[n_1, n_2])) + \frac{1}{2N}(\sum_{n_1,n_2}((y_e[n_1, n_2])) \quad , \tag{2.4}$$

where N is the number of image pixels.

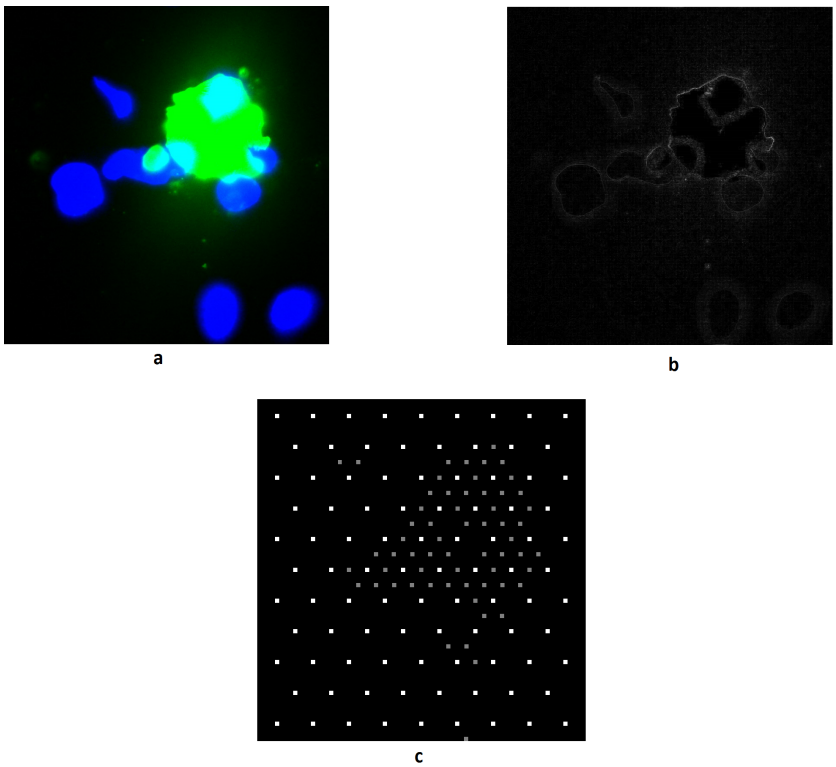


Figure 2.1: Seeding according to wavelet energy. (a) A MSC image, (b) wavelet energy image of (a), (c) seeded image according to wavelet energy.

This procedure can be repeated iteratively to increase the number of resolutions. However it is necessary to stop at some level otherwise we end up with too many small super-pixels with very few number of pixels. We can limit the number of pixels in a given image. As a result the threshold defined in Equation 2.4 can be increased or decreased according to a prespecified number of pixels.

In this work, two resolution levels are considered in which, super-pixel resolution is increased by four where average pixel resolution of each super-pixel is reduced to 1/4th of the original size as shown in Figure 2.2 (c). After this new seeding process, initial super-pixel groups are created by assigning pixels to the nearest cluster centers. In this thesis, a modified version of the SLIC clustering method [31] is used to read only the super-pixel boundaries. Similarly, the two distance measures in the SLIC algorithm are defined as:

$$d_c = \sqrt{(p_1 - m_1)^2 + (p_2 - m_2)^2 + (p_3 - m_3)^2} \quad , \tag{2.5}$$

and

$$d_l = \sqrt{(p_x - m_x)^2 + (p_y - m_y)^2} \quad , \tag{2.6}$$

where $d_c$ and $d_l$ are the distances of a pixel $p$ and super-pixel center in terms of color and position, in Equation 2.5 and 2.6 respectively. In Equation 2.5, $p_1$, $p_2$ and $p_3$ are the color values of pixel $p$, $m_1$, $m_2$ and $m_3$ are mean color values of the current super-pixel values, respectively. In Equation 2.6, $p_x$ and $p_y$ are the $x$ and $y$ position values of pixel $p$ in the image and $m_x$ and $m_y$ are the $x$ and $y$ position values of center of the given super-pixel, respectively. A weighted sum of $d_c$ and $d_l$ are used as a distance measure of each pixel into the center of super-pixels as follows:

$$d = \sqrt{d_c^2 + k.d_l^2.c} \quad , \tag{2.7}$$

where $k$ is a weight that calibrates the color and coordinate ranges. $c$ is the initial area property of the super-pixel and used in order to maintain the original size of the super-pixel. For each individual super-pixel, $c$ is calculated in the first iteration as:

$$c = \frac{1}{\sqrt{area}} \quad . \tag{2.8}$$

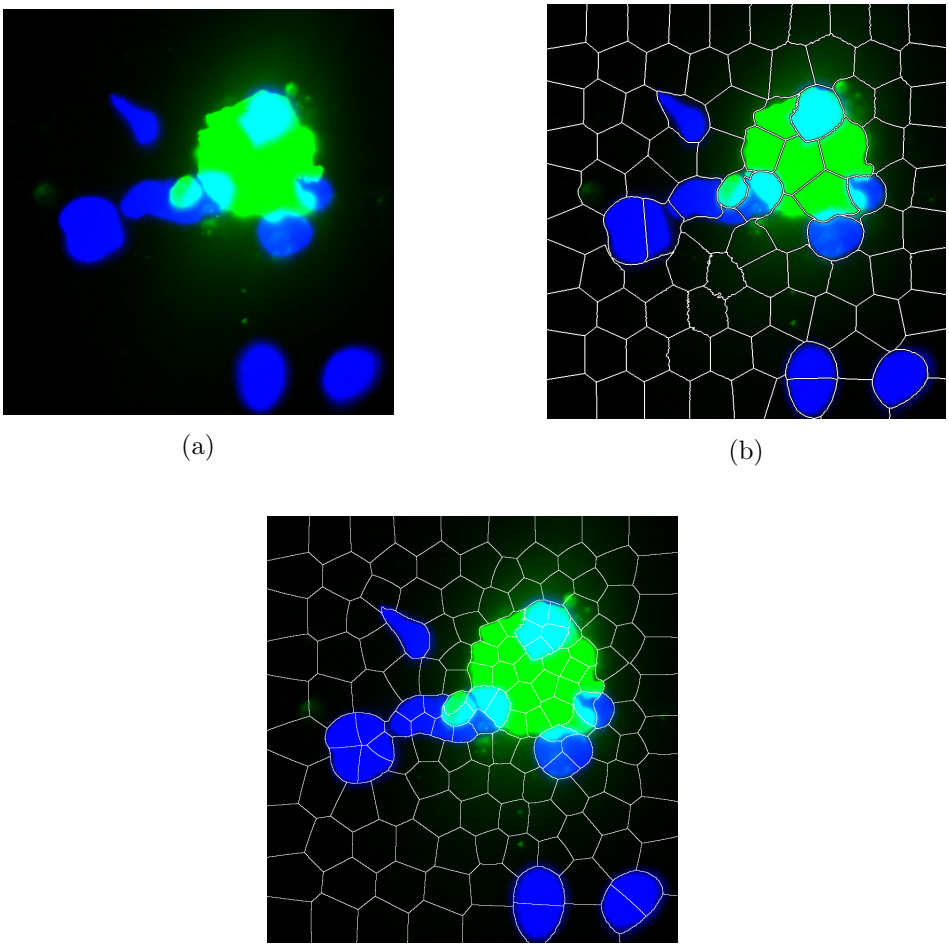

(a) (b)

(c)

Figure 2.2: Comparison of [SLIC](b) and proposed multi-resolution super-pixels algorithm (c).

For the image shown in Figure 2.2 (a), the result of the multi-resolution super-pixel clustering algorithm is shown in Figure 2.2 (c) for 200 initial seeds.

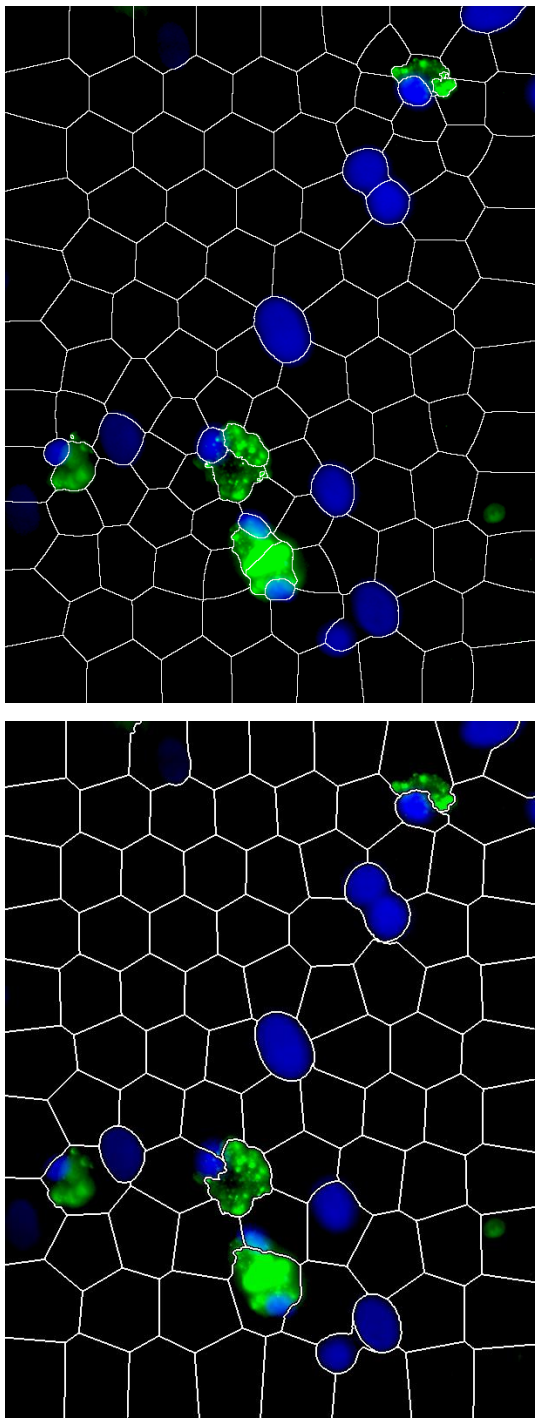

Figure 2.3: Comparison of proposed multi-resolution super-pixels algorithm (above) and SLIC algorithm (below).

## 2.2 Merging Algorithms for Super-Pixels

Merging algorithms for super-pixels are built for the unnecessary super-pixels in the image background. As it can be seen from Figures 2.2 and 2.3, super-pixels regions in the black background are unrelated with the cells. Therefore, two algorithms are implemented in order to get meaningful segmentation results by merging the similar super-pixels.

### 2.2.1 Merging Super-Pixels Using 1-D SIFT

SIFT [22], is a well known algorithm used in many computer vision applications [32–36]. The algorithm relies on extraction of local extrema and minima values. Images are filtered with Gaussian filters and the extrema points are obtained from Difference-of-Gaussian (DoG) images. Such extrema and minima points are used for the feature extraction process in many detection and restoration applications [37].

In the proposed approach, the aim is to merge similar super-pixels to determine the background of MSCs images. By differentiating background from the MSCs stem cells, these cells and their nuclei can be represented accurately. Therefore, an algorithm with the ability to match 1-D r,g,b color histograms to merge similar super-pixels is needed. A novel decision rule for merging neighboring super-pixels is developed using 1-D version of the SIFT algorithm. As in the 2-D SIFT method, 1-D histograms are filtered with 1-D Difference of Gaussian filters and local extrema locations are determined. The 32-binned histograms are compared to each other according to local extrema locations of DoG signals. The detection procedure of local extrema is similar to 2D SIFT. A point $x$ on a Difference of Gaussian scale is said to be an extrema if it is greater than the surrounding 8 points as shown in Figure 2.4 (in 2-D SIFT this number is 26).

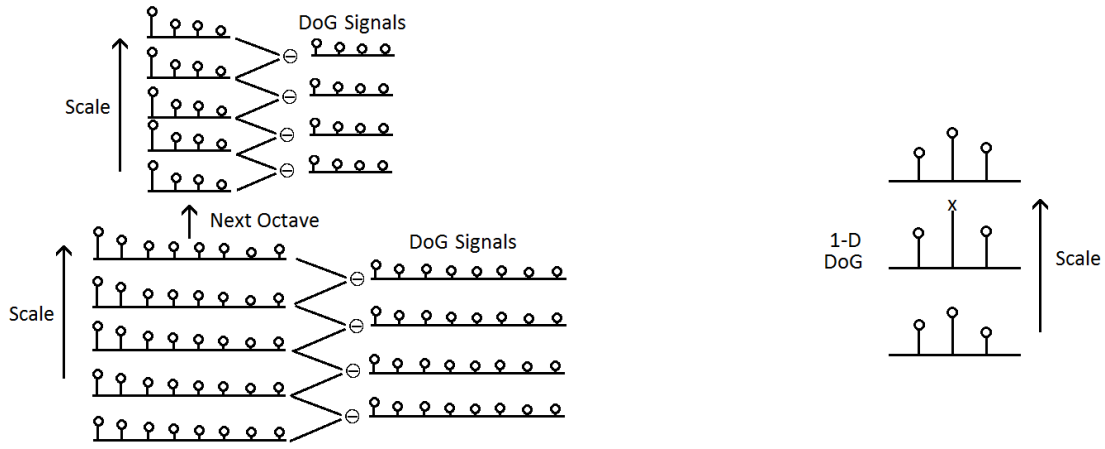


Figure 2.4: Extraction of extrema points in DoG histograms. After filtering the histograms with the Gaussian filters, a subtraction process took place and the DoG signals are constructed. Then a point $x$ is compared with its eight neighbors.

The matching criteria of neighboring super-pixels is to have similar SIFT extrema points in their histograms. Two super-pixels are considered to be similar as long as indexes of DoG extrema points are similar to each other. As a result, a 1-D SIFT based super-pixel or image region similarity method is developed. All one has to do is to set the number of matching extrema points for region similarity. In this way, a threshold-free similarity measurement becomes possible.

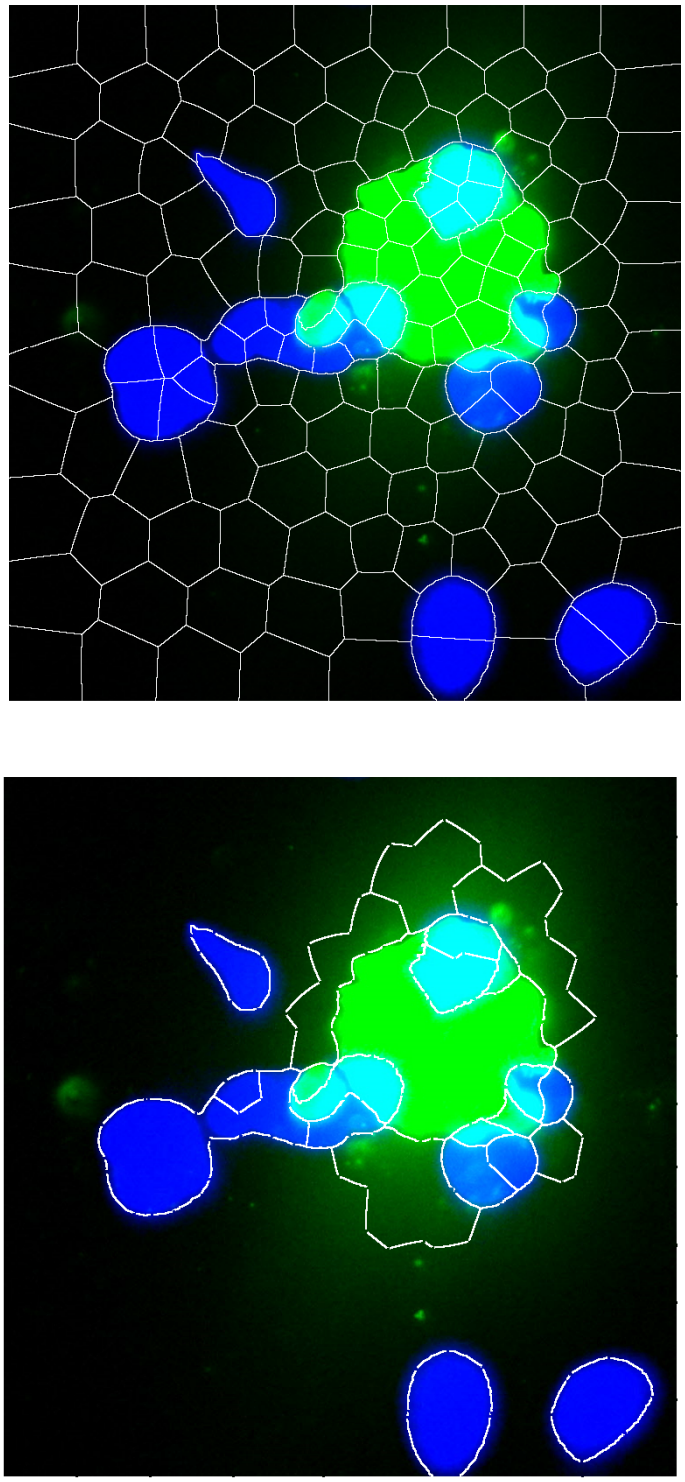

Figure 2.5: 1-D SIFT merging result.

### 2.2.2 Merging Super-Pixels Using Wavelets

Similar super-pixel regions can also be merged with the use of wavelets without using any threshold. Wavelets have many applications in image processing due to their ability to find frequency values without losing the time information [38–43]. In this study, histograms of color channels are used as input to compute the wavelet decomposition coefficients. In wavelet decomposition, low frequencies are generally calculated by projections onto scaling functions. On each level, input signals are projected onto a lower subspace. In the final level,the wavelet coefficient that is found for each channel is the DC value of the input signal.

When the histogram of color channel values of a constant number of pixels are used, it is expected that this DC value will be equal for every super-pixel regardless of the super-pixel colors. On lower levels of wavelet decomposition, these values vary depending on the color distribution. For two super-pixels with similar color distribution, it is expected for wavelet decomposition of their histograms to be similar in every level. Similarity of such super-pixels are measured by comparing the wavelet coefficient index of the largest wavelet coefficient in each level. Therefore on a wavelet decomposition level, the same indices of the largest wavelet coefficients of two super-pixels imply similarity. As the wavelet decomposition level decreases, the certainty of the similarity increases. It is also expected that if on a wavelet decomposition level, indices of the largest wavelet coefficients are the same for two super-pixels, such indices should be the same for higher levels of decomposition.

A histogram of R,G,B channel values for each super-pixel is calculated with $2^N$ bins. Having larger $N$ reduces the chances of the similarity index to be the same in lower levels (Here $N = 5$ is used). A histogram of each channel is processed separately. After dividing the color histograms of the two neighboring super-pixels into $2^N$ bins, we apply a low-pass filter (LPF) to all three color channels histograms:

$$h = \{\frac{1}{4}, \frac{1}{2}, \frac{1}{4}\} \quad . \tag{2.9}$$

It is not necessary to check the gain of such low pass filters since this algorithm compares only the index of the largest element in the wavelet coefficient series. If the index of the maximum value is equal for all three color channels, these two super-pixels will merge, if not, we decimate the histograms again and apply the same procedure.

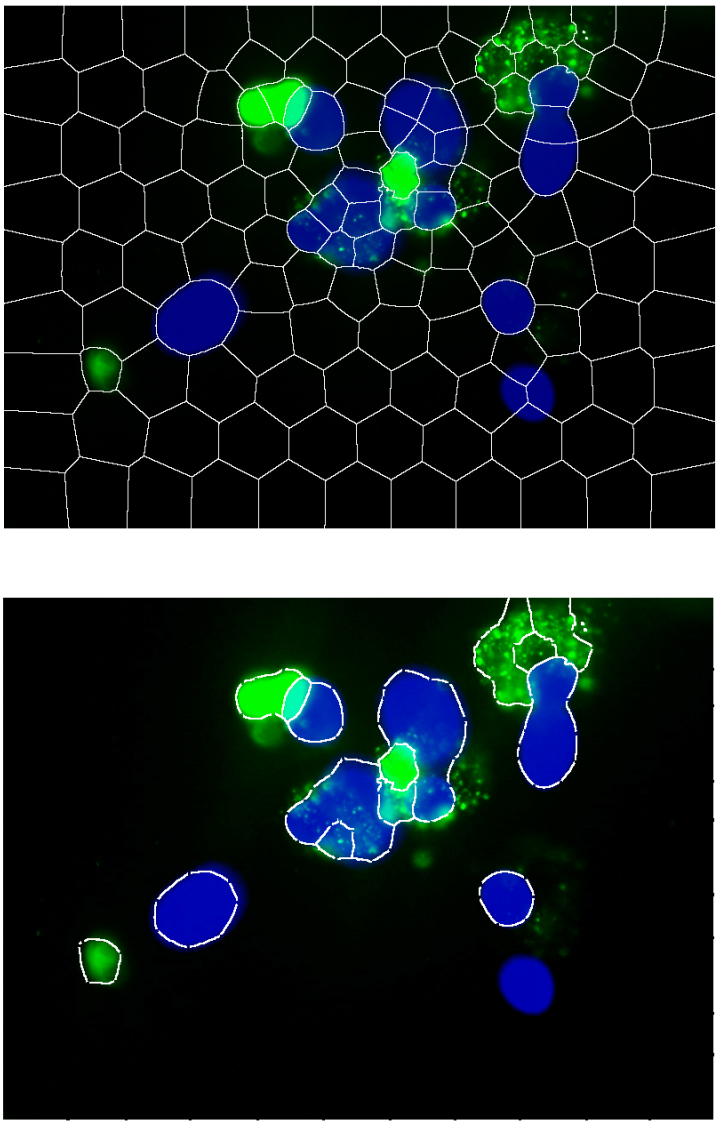

Figure 2.6: Wavelet merging result.

## 2.3 Experimental Results

Mesenchymal Stem Cell images used in this thesis are obtained by the Molecular Biology Department at Bilkent University.

The process of image acquisition is as follows: Bone marrow derived Mesenchymal Stem Cells (MSCs) were isolated from C56/BL6 mice. To label these cells, a new class of water-dispersible nanoparticle (CPN) was used. After 24 hour incubation of CPN, MSCs were fixed and visualized with fluorescence microscopy. The photos were taken with 10X-20X-40X magnification and the nucleus counter staining was done with DAPI. To have a more detailed perspective, a 40X magnification is used in general, however experiments for 10X and 20X are also considered. In the resulting images, green regions indicate cellular bodies (cytoplasm ) and blue regions indicate nucleus.

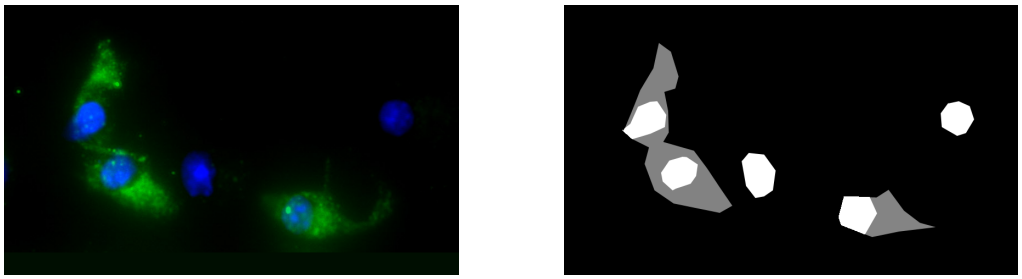

(a) A MSC image (b) The ground truth image of (a)

Figure 2.7: MSC image and the ground truth image of the same image.

First, MSC images are segmented into super-pixels by using the super-pixel algorithm in [31] and the proposed method. The initial number of super-pixels are given to be 100 for both algorithms. Detection and false alarm rates for each cell, nucleus and cytoplasm are calculated by comparing the results of the proposed algorithm and SLIC in [31] with manually marked regions of MSC images as ground-truth. 13 different MSC images are tested with an average resolution of 1000×800. Super-pixels are classified as cell-type or background-type depending on the region they cover in the ground-truth image. As shown in Figures 2.5

2.6, some cell-type super-pixels occupy background regions as well. Therefore, a super-pixel covering a larger background than the actual cell region is registered as background and vice versa.

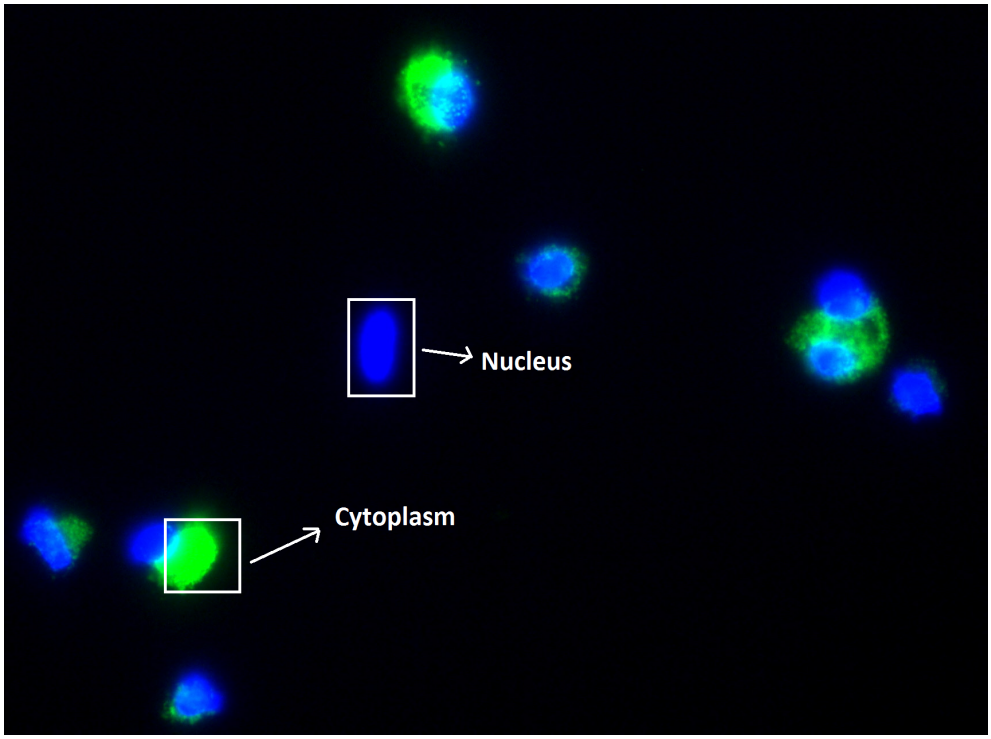


Figure 2.8: A MSC image taken under the fluorescence microscope. The green regions indicate cellular bodies (cytoplasm ) and the blue regions indicate nucleus.

The cell region detection accuracy of the proposed method is compared to the SLIC method [31] in Table 2.1.

Table 2.1: Comparison of cell detection in MSC images using multi-resolution super-pixels and SLIC.

| | Multi-resolution SP | SLIC |
|---|---|---|
| MSCs Image | Detection rate (%)/ False Alarm rate (%) | Detection rate (%)/ False Alarm rate (%) |
| Image 1 | 90.51 / 2.06 | 93.23 / 3.01 |
| Image 2 | 94.31 / 8.39 | 83.90 / 3.60 |
| Image 3 | 81.39 / 1.30 | 81.16 / 3.00 |
| Image 4 | 87.89 / 7.42 | 87.84 / 5.78 |
| Image 5 | 83.84 / 10.01 | 82.46 / 13.73 |
| Image 6 | 85.90 / 8.89 | 79.46 / 10.40 |
| Image 7 | 85.58 / 0.11 | 87.34 / 4.89 |
| Image 8 | 84.32 / 8.99 | 92.30 / 21.88 |
| Image 9 | 82.53 / 0.38 | 63.06 / 6.23 |
| Image 10 | 86.72 / 0.96 | 72.58 / 19.92 |
| Image 11 | 92.66 / 6.50 | 74.60 / 8.08 |
| Image 12 | 80.64 / 8.26 | 78.99 / 26.84 |
| Image 13 | 93.58 / 15.45 | 66.69 / 18.26 |
| Average | 86.91 / 6.05 | 80.04 / 11.20 |

As shown in Table 2.1, the proposed multi-resolution super-pixel algorithm is better in covering the cell region in MSC images. False alarm rates in Table 2.1 indicate that the SLIC algorithm cannot adapt to the changes in the cell borders. This is due to the fact that the contrast between the cells and the background is low at cell boundaries. The SLIC algorithm cannot detect such transitions. On the other hand, the proposed method can produce better results because of its multi-resolution nature. Nuclei detection results in MSC images are presented in Table 2.2.

Table 2.2: Nucleus region detection accuracy of the multi-resolution super-pixels method compared to the SLIC method.

| | Multi-resolution SP | SLIC |
|---|---|---|
| MSCs Image | Detection rate (%)/ False Alarm rate (%) | Detection rate (%)/ False Alarm rate (%) |
| Image 1 | 91.10 / 1.23 | 51.29 / 0.81 |
| Image 2 | 81.63 / 0.32 | 91.15 / 1.97 |
| Image 3 | 92.10 / 1.75 | 28.26 / 0.96 |
| Image 4 | 95.30 / 1.13 | 80.30 / 3.71 |
| Image 5 | 62.84 / 0.27 | 68.24 / 43.67 |
| Image 6 | 69.56 / 16.02 | 59.65 / 16.89 |
| Image 7 | 77.75 / 1.43 | 83.23 / 8.76 |
| Image 8 | 88.12 / 11.28 | 90.71/19.84 |
| Image 9 | 61.21 / 3.83 | 46.31 / 6.73 |
| Image 10 | 64.06 / 0.01 | 61.06 / 19.08 |
| Image 11 | 90.05 / 7.52 | 72.51 / 7.54 |
| Image 12 | 79.23 / 20.99 | 81.55 / 51.61 |
| Image 13 | 89.90 / 23.57 | 62.72 / 26.33 |
| Average | 80.21 / 6.87 | 67.46 / 15.99 |

In Table 2.2 it is observed that success rates of the multi-resolution super-pixel algorithm is greater then the success rates of the SLIC algorithm in nucleus detection. This is due to the advantage of starting with smaller super-pixels in the regions with high frequency components.

In addition to the comparison of the multi-resolution super-pixels with the SLIC algorithm, the 1-D SIFT and the wavelet merging algorithms are also compared. First, the ground truth images of the related MSC images are constructed. Then, these ground truth images are compared with the results of the 1-D SIFT and the wavelet merging algorithms separately. As a quality measure, Matthews Correlation Coefficient (MCC) results [44] are used. MCC is a balanced measure

for binary classification and can be used with different class sizes. In a simple manner it calculates the correlation between the observed and the predicted classification. It varies between minus one and one where one means perfect correlation and minus one means no correlation. MCC can be calculated as:

$$MCC = \frac{(TP)(TN)-(FP)(FN)}{\sqrt{(TP+FP)(TP+FN)(TN+FP)(TN+FN)}} \quad , \tag{2.10}$$

where FP,FN TP and TN stands for false positive, false negative, true positive and true negative respectively.

The balanced F1 measure [45] is used to compare the accuracies of both methods. It is a harmonic mean of Precision and Recall where values of the score vary between zero and one. Balanced F1 score can be defined as:

$$F1 = 2 \times \frac{Precision \times Recall}{Precision + Recall} \quad , \tag{2.11}$$

where precision and recall are defined as:

$$Precision = \frac{TP}{TP+FP} \quad , \tag{2.12}$$

$$Recall = \frac{TP}{TP+FN} \quad . \tag{2.13}$$

In addition to the metrics above,both specificity and accuracy of each merging method are calculated. Specificity and accuracy are obtained as :

$$Specificity = \frac{TP}{TP+FP} \quad , \tag{2.14}$$

$$Accuracy = \frac{TP+TN}{TP+FP+FN+TN} \quad . \tag{2.15}$$

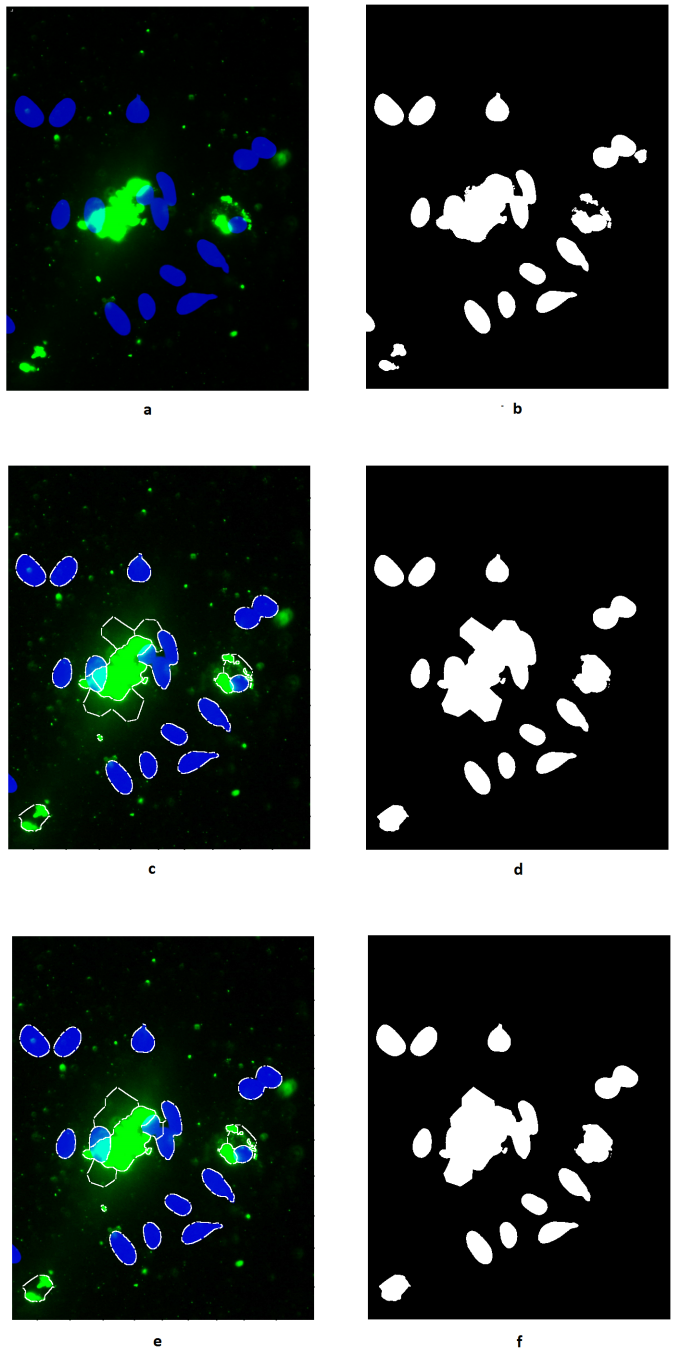


Figure 2.9: (a) MSC image # 10, (b) the ground truth image of (a), (c) 1-D SIFT merging result, (d) area captured after 1-D SIFT merging, (e) Wavelet merging result, (f) area captured after wavelet merging.

Table 2.3: 1-D SIFT merging results for MSC images.

| Image | MCC | F1 | Specificity | Recall | Precision | Accuracy |
|---|---|---|---|---|---|---|
| Image 1 | 0.65 | 0.67 | 0.98 | 0.59 | 0.77 | 92.55 |
| Image 2 | 0.72 | 0.72 | 0.99 | 0.61 | 0.89 | 92.70 |
| Image 3 | 0.72 | 0.75 | 0.90 | 0.95 | 0.62 | 82.37 |
| Image 4 | 0.56 | 0.56 | 0.86 | 0.95 | 0.39 | 75.16 |
| Image 5 | 0.71 | 0.74 | 0.97 | 0.72 | 0.76 | 89.36 |
| Image 6 | 0.69 | 0.73 | 0.94 | 0.77 | 0.70 | 84.28 |
| Image 7 | 0.83 | 0.87 | 0.99 | 0.78 | 0.98 | 84.60 |
| Image 8 | 0.82 | 0.84 | 0.98 | 0.77 | 0.92 | 91.31 |
| Image 9 | 0.76 | 0.76 | 0.99 | 0.62 | 0.98 | 89.68 |
| Image 10 | 0.82 | 0.84 | 0.99 | 0.75 | 0.94 | 92.04 |
| Image 11 | 0.90 | 0.90 | 0.99 | 0.85 | 0.95 | 98.53 |
| Image 12 | 0.61 | 0.59 | 0.98 | 0.44 | 0.88 | 94.79 |
| Image 13 | 0.88 | 0.88 | 0.99 | 0.87 | 0.90 | 96.84 |

Table 2.4: Wavelet merging results for MSC images.

| Image | MCC | F1 | Specificity | Recall | Precision | Accuracy (%) |
|---|---|---|---|---|---|---|
| Image 1 | 0.63 | 0.64 | 0.98 | 0.55 | 0.78 | 92.28 |
| Image 2 | 0.73 | 0.73 | 0.99 | 0.59 | 0.95 | 93.18 |
| Image 3 | 0.76 | 0.78 | 0.99 | 0.66 | 0.94 | 89.41 |
| Image 4 | 0.85 | 0.86 | 0.99 | 0.76 | 0.98 | 95.92 |
| Image 5 | 0.74 | 0.75 | 0.99 | 0.65 | 0.90 | 91.02 |
| Image 6 | 0.81 | 0.82 | 0.99 | 0.73 | 0.95 | 91.21 |
| Image 7 | 0.86 | 0.89 | 0.99 | 0.81 | 0.99 | 87.24 |
| Image 8 | 0.80 | 0.82 | 0.99 | 0.73 | 0.94 | 90.71 |
| Image 9 | 0.76 | 0.76 | 0.99 | 0.62 | 0.98 | 89.68 |
| Image 10 | 0.81 | 0.82 | 0.99 | 0.72 | 0.96 | 91.67 |
| Image 11 | 0.90 | 0.90 | 0.99 | 0.85 | 0.95 | 98.53 |
| Image 12 | 0.61 | 0.59 | 0.99 | 0.85 | 0.95 | 98.53 |
| Image 13 | 0.88 | 0.88 | 0.99 | 0.87 | 0.90 | 96.84 |

In Tables 2.3 and 2.4, MCC, F1, Specificity, Recall, Precision and Accuracy results are given for both merging methods. Although, both methods have very close results, the wavelet merging algorithm gives better performance in MCC and F1 scores.

# Chapter 3

# Applications on CD13 and H&E Stained Cancer Tissue Images

## 3.1 Detection of Cancer Stem Cells in Microscopic Images by Using Region Covariance and Co-difference Method

In this thesis, co-difference and covariance methods are used as image region descriptors. The region covariance method for feature extraction is a well studied method for human detection, object detection and image retrieval [23, 46–49]. In [23], it is shown that covariance matrix method can be used as an image region descriptor and gives better performance than the previous approaches to detection and recognition problems. In [50], eigenvalues of the covariance matrix are used for corner detection.

The co-difference method is the modified version of the covariance method [24]. Instead of using multiplication, it uses its own novel vector product definition that permits a multiplier-free implementation to overcome the multiplication cost. It

is shown that this method can be used for constructing a so-called region co-difference matrix that has very similar properties to the region covariance matrix and can be used in many different applications [51–53].

### 3.1.1 Covariance Region Descriptor

Let $f_k$ be the feature vector of a pixel $I(x, y)$ with the dimension of $d$. When we index the image pixel with a single index $k$, with the assumption that we have $N$ number of pixels in a given region, the index $k$ takes the values $k = 1....N$. The covariance descriptor for this image is calculated as:

$$C_V = \frac{1}{N-1} \sum_{k=1}^{N} (f_k - \bar{\mu}) \times (f_k - \bar{\mu})^T \quad . \tag{3.1}$$

The mean vector, $\bar{\mu}$ is the vector where the mean values of the extracted feature vectors are kept. Since the covariance matrix is symmetric, the number of the independent variables are $d(d+1)/2$ [24].

### 3.1.2 Co-difference Region Descriptor

Although the calculation cost of a single covariance matrix is not too high, as the number of covariance matrices increase, it escalates. The co-difference matrix presented in [24] reduces this cost. That is:

$$C_D = \frac{1}{N-1} \sum_{k=1}^{N} (f_k - \bar{\mu}) \oplus (f_k - \bar{\mu})^T \quad . \tag{3.2}$$

The operator "$\oplus$" is defined in [24] as an additive operator which is used instead of the scalar multiplication used in Equation 3.1. Loosely speaking, it behaves like a matrix multiplication operation, despite being an addition operation. Due to the sign of the outcome, it acts like a multiplication operation. The

operation "$\oplus$" between real numbers $a$ and $b$ is defined as in [24] below:

$$a \oplus b = \begin{cases} a + b & \text{if } a \geq 0 \text{ and } b \geq 0 \\ a - b & \text{if } a \leq 0 \text{ and } b \geq 0 \\ -a + b & \text{if } a \geq 0 \text{ and } b \leq 0 \\ -a - b & \text{if } a \leq 0 \text{ and } b \leq 0 \end{cases} \quad , \tag{3.3}$$

where Equation 3.3 can be expressed as follows:

$$a \oplus b = \text{sign}(a \times b)(|a| + |b|) \quad . \tag{3.4}$$

Like the covariance matrix, the co-difference matrix is symmetric due to the symmetry property of $\oplus$ operator, where $a \oplus b = b \oplus a$. Also, if the two values have the same sign, the co-difference between them will be positive and vice versa.

### 3.1.3 Feature Extraction from Image Regions

A feature vector is extracted from each pixel and used in construction of the region covariance and the co-difference matrices. The feature vectors are extracted from overlapping windows of size 11×11 pixels. The structure of the feature vector is defined as:

$$f_k = \left[R(x,y), G(x,y), B(x,y), \frac{dR(x,y)}{dx}, \frac{dR(x,y)}{dy}, \frac{d^2R(x,y)}{dx^2}, \frac{d^2R(x,y)}{dy^2}\right] \quad , \tag{3.5}$$

where $R(x,y)$, $G(x,y)$ and $B(x,y)$ are the pixel values at $(x,y)$ positions in red, green and blue channels, respectively. The last four elements of the feature vector are the first and second derivatives of the red channel with respect to x and y coordinates. Our aim is to find CSC's in CD13 stained images. In these images CSC appear as a dark brown color. Since the brown color is dependent on the red channel more than the other two channels, we consider the red channel derivatives

in our feature vector. Covariance , $C_V$, and co-difference, $C_D$, matrices are derived from the extracted feature vector as in Equation 3.1 and 3.2.

In Equation 3.1 and 3.2, $N$ is the total number of pixels in a window. That makes 121 for a given 11×11 window. The mean vector, $\bar{\mu}$, is defined as follows:

$$\bar{\mu} = \left[\mu(I_R), \quad \mu(I_G), \quad \mu(I_B), \quad \mu(\frac{dI_R}{dx}), \quad \mu(\frac{dI_R}{dy}), \quad \mu(\frac{d^2I_R}{dx^2}), \quad \mu(\frac{d^2I_R}{dy^2})\right] \quad , \tag{3.6}$$

where $I_R$, $I_G$, $I_B$ represents the image pixels in the red, green, and blue channels. The mean operation, $\mu : \mathbb{Z}^2 \to \mathbb{Z}$, takes the mean of given pixels. The extracted mean values are kept as a vector $\bar{\mu}$.

After the feature vectors are extracted from the pixels, corresponding covariance and co-difference matrices are constructed.

$$C_{ROI} = \begin{bmatrix} C_{1,1} & \cdots & C_{1,7} \\ \vdots & \ddots & \vdots \\ C_{7,1} & \cdots & C_{7,7} \end{bmatrix} \tag{3.7}$$

In Equation 3.7, $C_{ROI}$ represents the calculated $C_V$ or $C_D$ matrices. Here only the lower triangle values are taken into account because of the symmetry. The values of the lower triangle area are placed into a vector with the size of 1 x 28. The 11×11 regions are represented with this $z_k$ vector. Where $z_k$ is defined as:

$$z_k = [C_{1,1}, C_{2,1}, C_{2,2}, C_{3,1}, C_{3,2}, C_{3,3} \cdots, C_{7,6}, C_{7,7}] \quad . \tag{3.8}$$

To increase accuracy we add the mean color values to the end of the feature vector:

$$z_k = [C_{1,1}, C_{2,1}, C_{2,2}, \cdots, C_{7,7}, \mu(I_R), \mu(I_G), \mu(I_B)] \quad . \tag{3.9}$$

### 3.1.4 Experimental Results

In the experimental process, liver cancer tissue images which stained with CD13 dye are used. In these images, cancer stem cells have unique dark brown colors where cancer cells have bright blue colors as shown in Figure 3.1.

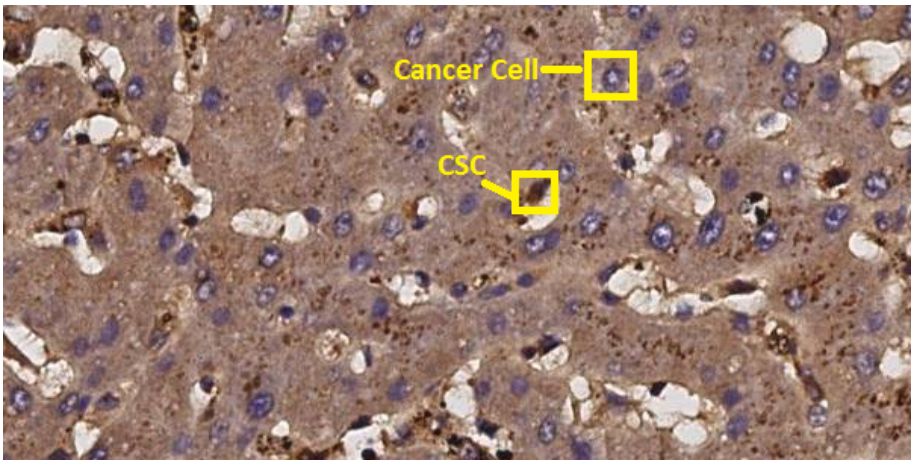


Figure 3.1: A liver cancer tissue stained using CD13 primary antibodies.

Our CSC image data set is constructed as follows: In total 600 cell images are taken from three CD13 images, both for stem cells and for the other image regions. 11×11 windows are used to select these regions. The feature vectors of 121 pixels are calculated separately and then for each cell window, covariance and the co-difference descriptors are constructed. In the end, we get 600 covariance and 600 co-difference data matrices. $z_k$'s are calculated from this data and used as a ground truth.

The ground truth data is mapped between [0-1] and then fed into SVM [54]. Since we only have two classes it is a binary classification problem and models are trained with the LIBSVM [55] tool with the Radial Basis Function (RBF) kernel. The best gamma and C parameters of the RBF kernel are selected via grid search. We used 70% of our ground truth data for training and 30% for testing our models. Testing accuracies for our two models are given in Table 3.1

below.

Table 3.1: SVM test accuracies.

| | Co-difference Model | Covariance Model |
|---|---|---|
| Accuracy (%) | 99.79 | 96.66 |

A sliding window model with size 11×11 is constructed. While the overlapping window sweeps through the image, the data inside the window is processed with both methods. Processed data is predicted with the models separately. According to the prediction result, the predicted window is marked. In Table 3.2 marked cells are counted and compared with the ground truth image.

Table 3.2: Number of detected cells by each method.

| Image # | True CSC | Detected by CoD | Detected by CoV | False CoD Detection | False CoV Detection |
|---|---|---|---|---|---|
| CD13-1 | 38 | 37 | 37 | 88 | 75 |
| CD13-2 | 63 | 59 | 62 | 50 | 52 |
| CD13-3 | 37 | 28 | 28 | 27 | 48 |
| CD13-4 | 76 | 73 | 75 | 65 | 69 |
| CD13-5 | 24 | 24 | 24 | 49 | 54 |
| CD13-6 | 52 | 52 | 52 | 68 | 79 |
| CD13-7 | 114 | 106 | 111 | 8 | 8 |
| CD13-8 | 66 | 64 | 66 | 8 | 5 |
| CD13-9 | 78 | 55 | 67 | 3 | 0 |
| CD13-10 | 92 | 71 | 81 | 37 | 45 |
| CD13-11 | 23 | 16 | 17 | 4 | 14 |
| CD13-12 | 64 | 21 | 44 | 4 | 169 |
| CD13-13 | 64 | 58 | 60 | 118 | 116 |

In Table 3.2, for the CD13-10 image, the co-difference method finds a total of 108 cell of which 71 are true detection. For the same image, the covariance method finds 126 cells of which 45 are false detection. In Figure 3.2, the CD13-10 image and its predicted versions are shown. Clearly, although the covariance method seems to detect more cells, the true detection rate is low. Thus, to measure the

quality and the accuracy in a more meaningful manner, Matthews Correlation Coefficient (MCC) and F1 scores are used as explained in Chapter 2.

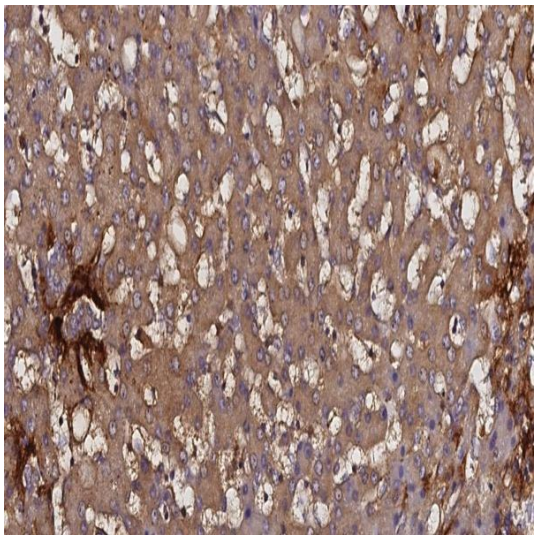

(a) CD13-10 image

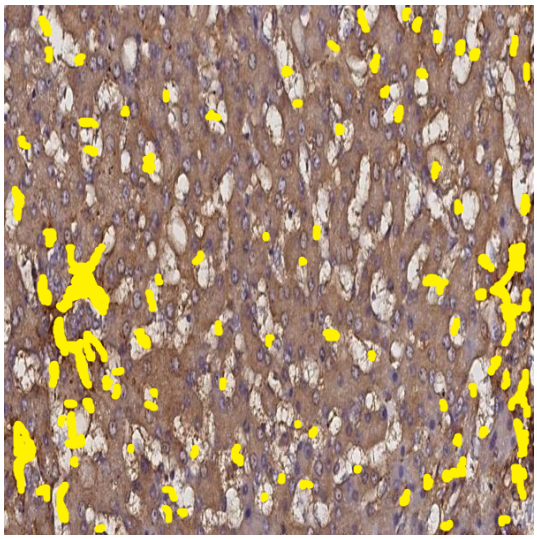

(b) Ground truth of CD13-10

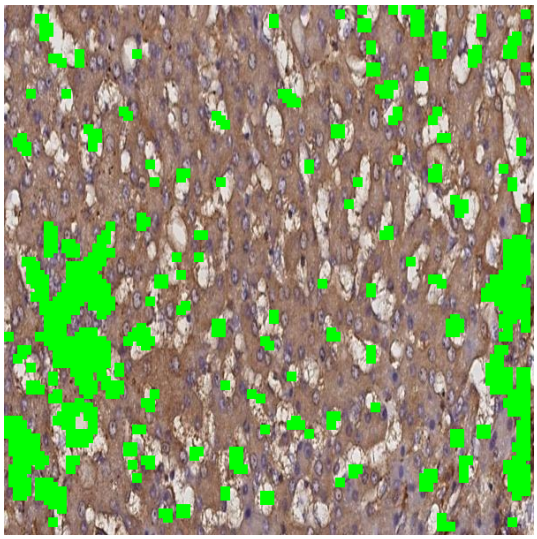

(c) Co-difference method result for CD13-10

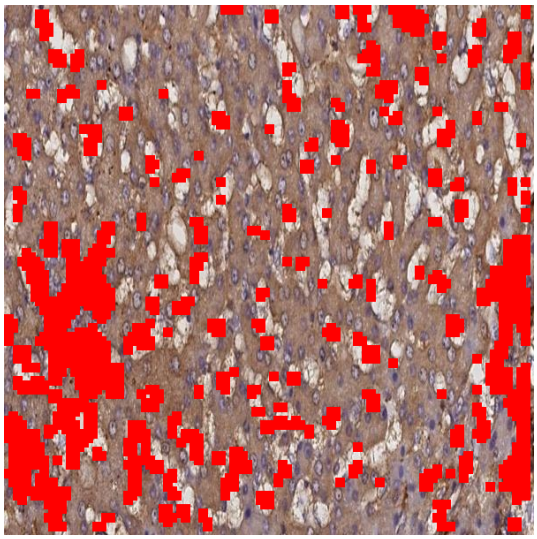

(d) Covariance method result for CD13-10

Figure 3.2: Comparison of covariance and co-difference algorithms. A CD13 stained image (a), its ground truth image marked by a pathologist (b), the result of the co-difference method (c),the result of the covariance method (d).

Table 3.3: MCC scores of the images.

| | Co-difference MCC | Covariance MCC |
|---|---|---|
| CD13-1 | 0.23 | 0.23 |
| CD13-2 | 0.42 | 0.40 |
| CD13-3 | 0.43 | 0.39 |
| CD13-4 | 0.41 | 0.34 |
| CD13-5 | 0.40 | 0.39 |
| CD13-6 | 0.40 | 0.37 |
| CD13-7 | 0.43 | 0.39 |
| CD13-8 | 0.47 | 0.41 |
| CD13-9 | 0.41 | 0.44 |
| CD13-10 | 0.44 | 0.41 |
| CD13-11 | 0.54 | 0.53 |
| CD13-12 | 0.23 | 0.21 |
| CD13-13 | 0.23 | 0.22 |
| CD13-14 | 0.36 | 0.36 |
| CD13-15 | 0.60 | 0.60 |
| CD13-16 | 0.77 | 0.76 |
| CD13-17 | 0.79 | 0.80 |
| CD13-18 | 0.77 | 0.76 |

MCC score results for both methods are compared and shown in Table 3.3. As it can be seen from the Table 3.3 that, co-difference method achieves finer results than covariance method.

In Table 3.4, F1 scores of both methods are compared. It is observed that using the co-difference method leads to better results by means of F1 score (13 out of 18).

Table 3.4: F1 scores of the images.

| | Co-difference F1 | Covariance F1 |
|---|---|---|
| CD13-1 | 0.13 | 0.13 |
| CD13-2 | 0.37 | 0.32 |
| CD13-3 | 0.41 | 0.30 |
| CD13-4 | 0.38 | 0.32 |
| CD13-5 | 0.31 | 0.29 |
| CD13-6 | 0.32 | 0.28 |
| CD13-7 | 0.40 | 0.28 |
| CD13-8 | 0.41 | 0.35 |
| CD13-9 | 0.49 | 0.46 |
| CD13-10 | 0.46 | 0.38 |
| CD13-11 | 0.55 | 0.52 |
| CD13-12 | 0.14 | 0.14 |
| CD13-13 | 0.13 | 0.12 |
| CD13-14 | 0.26 | 0.25 |
| CD13-15 | 0.66 | 0.66 |
| CD13-16 | 0.80 | 0.81 |
| CD13-17 | 0.82 | 0.67 |
| CD13-18 | 0.81 | 0.80 |

## 3.2 Mixture of Online Learners for Cancer Stem Cell Detection in CD13 Stained Microscopic Images

Pathologists can detect cancer stem cells from immunohistochemical cancer tissue slides stained with CD13 marker under the microscope. The microscopic images of CSCs and cancer cells appear as dark brown and blue respectively. These regions are indicated in Figure 3.3. Pathologists identify the CSCs to determine the severity of the cancer. The purpose is to make this process more reliable

and reduce human based errors. Implemented algorithm linearly combines the results of region covariance and region co-difference algorithms, and displays CSC marked regions to the pathologist. Since the tissue microarray (TMA) images are large, only a small portion of the tissue is displayed on the monitor. If the pathologists want to correct the automatically marked regions, they mark incorrectly determined CSC regions and/or undetected CSC regions on the screen manually. Based on the feedback given by the pathologists, weights of the individual learners are updated using a Least Mean Square (LMS) based online learning algorithm. Then, the entire tissue image is marked and quantified again using the updated weights.

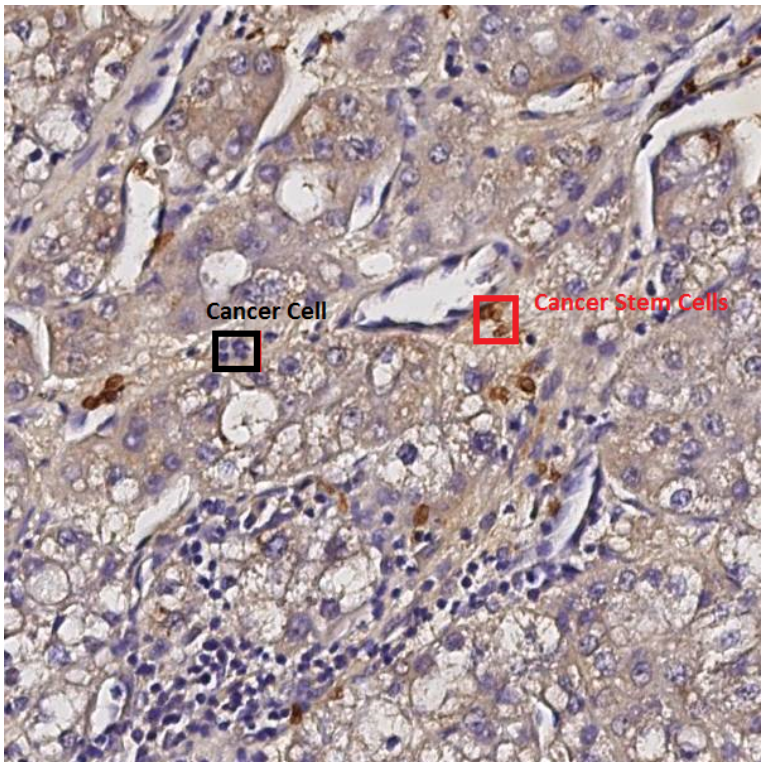


Figure 3.3: Immunohistochemistry (IHC) images of liver cancer tissue stained using CD13 primary antibodies.

### 3.2.1 Feature Extraction

Similar to Section 3.1 region covariance and region co-difference descriptors are used for representing the image regions. A feature vector is extracted from each pixel and used in construction of the region covariance and the co-difference matrices. Again, the feature vectors are extracted from overlapping windows of size 11×11 pixels. The structure of the feature vector is as follows:

$$f_k = \big[R(x,y), \quad G(x,y), \quad B(x,y), \frac{dR(x,y)}{dx}, \frac{dR(x,y)}{dy}, \frac{d^2R(x,y)}{dx^2}, \frac{d^2R(x,y)}{dy^2}\big] \quad , \tag{3.10}$$

where $R(x,y)$, $G(x,y)$ and $B(x,y)$ are the pixel values at $(x,y)$ positions in red, green and blue channels, respectively. The last four elements of the feature vector are the first and second derivatives of the red channel with respect to x and y. The covariance matrix, $C_V$, and codifference, $C_D$, are derived from the extracted feature vector as in Equation 3.11 and 3.12:

$$C_V = \frac{1}{N-1}\sum_{k=1}^{N}(f_k - \bar{\mu}) \times (f_k - \bar{\mu})^T \quad , \tag{3.11}$$

$$C_D = \frac{1}{N-1}\sum_{k=1}^{N}(f_k - \bar{\mu}) \oplus (f_k - \bar{\mu})^T \quad . \tag{3.12}$$

In Equation 3.11 and 3.12, $N$ is the number of pixels. This is 121 for given a 11×11 window. The mean vector, $\bar{\mu}$, is defined as:

$$\bar{\mu} = \big[0, \quad 0, \quad 0, \quad \mu(\frac{dI_R}{dx}), \quad \mu(\frac{dI_R}{dy}), \quad \mu(\frac{d^2I_R}{dx^2}), \quad \mu(\frac{d^2I_R}{dy^2})\big] \quad , \tag{3.13}$$

where $I_R$ represents the image pixels in the red channel. The mean operation, $\mu : \mathbb{Z}^2 \to \mathbb{Z}$, computes the mean of pixels in a given window. The extracted mean

values are kept as a vector $\bar{\mu}$. The first three elements of $\bar{\mu}$ are taken as zero in order to preserve the pixel color information after the extraction in Equation 3.11. It is experimentally observed that constructing $\bar{\mu}$ as in Equation 3.13 produces better detection results.

As in Section 3.1, the $C_{ROI}$ matrix, which represents the calculated $C_V$ or $C_D$ matrices is calculated and the values of the lower triangle area are again used to construct the feature vector with the size of 1 x 28. The regions are represented with this $z_k$ vector as:

$$z_k = [C_{1,1}, C_{2,1}, C_{2,2}, C_{3,1}, C_{3,2}, C_{3,3} \cdots, C_{7,6}, C_{7,7}] \quad . \tag{3.14}$$

Note that color mean values are not added at the end of $z_k$ as in Section 3.1. In addition to the region covariance and the co-difference descriptors, mean values of R, G, B, Y, Cb, Cr, H ,S, V, channels are also extracted from corresponding 11×11 windows and used as feature vectors. To sum up, from a 11×11 window we extract five feature vectors: $z_k$'s for both the covariance and the co-difference region descriptors and three separate mean value feature vectors corresponding to each color space.

### 3.2.2 Mixture of Learners (MoL) Algorithm

The Mixture of Learners (MoL) method combines the trained machine learning models to achieve the best CSC classification in CD13 images. First, the entire image is scanned with an overlapping window of size 11×11 pixels. The feature vectors mentioned in Section 3.2.1 are obtained from these windows. The size of the feature vector depends on the region description method. These feature vectors of the same type are concatenated to construct a feature matrix which represents the whole image. Therefore, five different feature matrices are constructed for a single image. Each row of these matrices are fed into the learners shown as Learner $N$ in Figure 3.4. The predictions, $L_p(n), n \in (1, ..., N)$, for each window are obtained separately. $L_p(n)$ is one for positive detection and minus

one for otherwise. In our implementation we have ten learners, thus the number of maximum learners $N$ is 10.

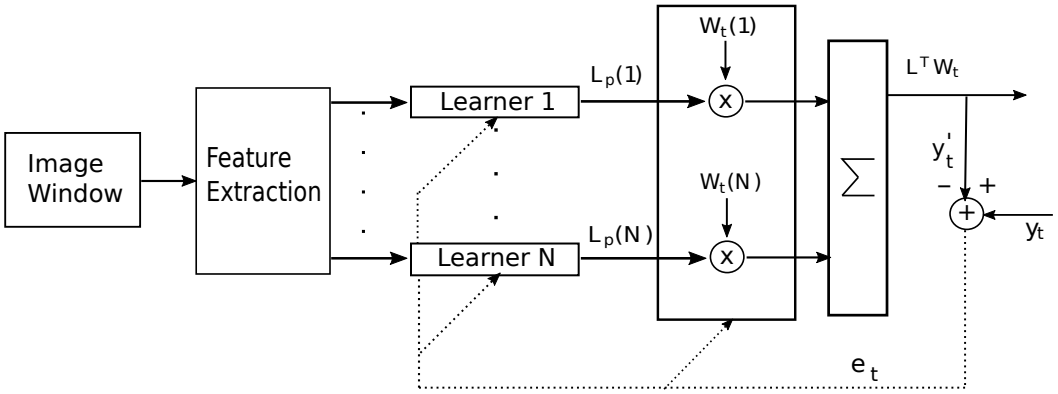


Figure 3.4: Mixture of learners block diagram.

In Figure 3.4, the block diagram of MoL algorithm is presented. In the MoL algorithm, the feature vectors are extracted from the image windows and fed into the related prediction model. Prediction results of the each model are multiplied with an initial weight vector $W_t$ and then linearly combined as $L^T W_t$. After the first run, the predicted image is shown to the user via Graphical User Interface (GUI). The user indicates the incorrectly marked regions with a marking tool in the GUI. According to this feedback of the user $y_t$, the system updates the weights of individual learners $W_t$. A gradient descent type algorithm is used to update the weights as follows:

$$W_{t+1} = W_t + \frac{e_t}{\|L\|^2} L \quad , \tag{3.15}$$

where $W_{t+1} = [w_{t+1,1}, \ldots, w_{t+1,10}]^T$ is the updated weight vector at time $t+1$, $W_t = [w_{t,1}, \ldots, w_{t,10}]^T$ is the current weight vector at time $t$. $L$ is the decision vector of the learners defined as $L = [L_p(1), L_p(2), \ldots, L_p(10)]$ and $e_t$ is the loss (or error) which is defined as:

$$e_t = y_t - y'_t \quad , \tag{3.16}$$

where the $y'_t$ is the current predicted value calculated from $L^T W_t$ as shown in Figure 3.4. The algorithm works with the updated weights and repeats until the user decides to stop this process.

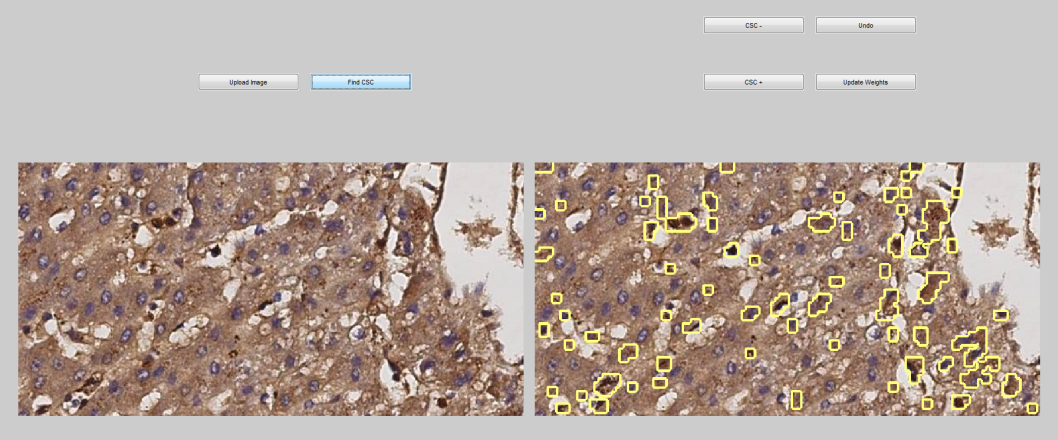


Figure 3.5: The implemented graphical user interface (GUI).

In some cases the weight update process fails to classify some regions indicated by the user of the GUI. In order to achieve the desired output, $L$ is expanded with additional information. The additional information represents a distance measure between that region and all regions in the image. The distance between two regions is calculated using co-difference values in [56]:

$$d(C_1, C_2) = \sum_{i=1}^{p} \left[ \sum_{j=1}^{p} \frac{|C_1(i,j) - C_2(i,j)|}{(C_1(i,i) + C_2(i,i))} \right] \quad . \tag{3.17}$$

After the distances between the desired region, which could not be correctly classified and all other regions are calculated, a sigmoid function is used to map the distances to values (v) between 0 and 1 and defined as:

$$sigm(d) = \frac{1}{1 + e^{-a(x-c)}} \quad , \tag{3.18}$$

where $c = 0.5$ and $a = -8$. However, the desired region could be *not a CSC* (label : -1) or *CSC* (label : 1) region. Thus, $v$ is multiplied by the desired label

to indicate the class information. This information is then added to the decision vector $L$. The new column added to $L$ and a weight that is independent from the weight update process is assigned to it. Moreover, the co-difference values of the desired region, which could not be correctly classified are saved along with the desired label. This is necessary to be able to compute the distances when another image is used as input to the system.

### 3.2.3 Experimental Setup and Results

The serial sections of tissue marker array (TMA) samples of liver cancer were purchased from US BioMAX (`http://www.biomax.us/tissue-arrays`). The paraffin embedded TMA tissues were deparaffinized and stained with a Dako EnVision kit using CD13 primary antibodies in 1:500 dilutions. Finally, immunohistochemistry stained TMA samples were analyzed under a light microscope (EUROMEX-Oxion). The images which are utilized in ground truth data extraction are in 20X magnification with the size 600x600 pixels. Our CSC data set is constructed as follows: In total 840 windowed regions from seven CD13 images are taken for both CSC and other image regions. Images are normalized between zero and one. Since the co-difference operation is a non-linear operation, it causes loss of information after the normalization. Therefore, the normalization is done for all feature extraction cases except for the co-difference case. In Support Vector Machines (SVM), Radial Basis Function (RBF) kernel and 5-fold cross validation is applied by using the LiBSVM tool [55]. The best parameters for RBF kernel such as $C$ and $\gamma$ are selected via grid search. Neural Networks (NN) are built with the MATLAB®'s Artificial Neural Networks (ANN) application for pattern recognition. The number of hidden layers in the NN are taken as 10 and *scaled conjugate gradient back propagation* is used. We divide 60% of our data for training, 20% for cross-validation and 20% for the test phase.

Table 3.5: SVM model information of the region descriptors.

| Method | Accuracy (%) |
|---|---|
| Covariance SVM | 97.61 |
| Co-Difference SVM | 98.08 |
| RGB-Mean SVM | 98.21 |
| YCbCr-Mean SVM | 95.83 |
| HSV-Mean SVM | 97.61 |

Table 3.6: Neural network model information of the region descriptors.

| Method | Accuracy (%) | Cross Entropy |
|---|---|---|
| Covariance NN | 97.00 | 2.97461 |
| Co-Difference NN | 96.40 | 1.68052 |
| RGB-Mean NN | 98.20 | 2.17499 |
| YCbCr-Mean NN | 97.00 | 2.63928 |
| HSV-Mean NN | 98.80 | 2.15902 |

Accuracies of the trained models in the test set are shown in Tables 3.5 and 3.6. To measure the test quality and test accuracy Matthews Correlation Coefficient (MCC) [44] and F1 score [45] are used respectively.

Table 3.7: Average classification results.

| Method | MCC | F1 | Specificity | Recall | Precision |
|---|---|---|---|---|---|
| Co-Difference SVM | 0.2916 | 0.2720 | 0.9743 | 0.3019 | 0.4219 |
| Covariance SVM | 0.4175 | 0.3883 | 0.9757 | 0.4062 | 0.5774 |
| Co-Difference NN | 0.3444 | 0.2977 | 0.9964 | 0.2164 | 0.6581 |
| Covariance NN | 0.2251 | 0.2298 | 0.9510 | 0.3750 | 0.1798 |
| RGB-Mean SVM | 0.4463 | 0.4255 | 0.9605 | 0.5155 | 0.5074 |
| RGB-Mean NN | 0.4090 | 0.3622 | 0.9947 | 0.2858 | 0.7216 |
| YCbCr-Mean SVM | 0.4407 | 0.4173 | 0.9654 | 0.4843 | 0.5316 |
| YCbCr-Mean NN | 0.4341 | 0.4024 | 0.9913 | 0.3513 | 0.6619 |
| HSV-Mean SVM | 0.4278 | 0.3961 | 0.9892 | 0.3546 | 0.6471 |
| HSV-Mean NN | 0.4046 | 0.3636 | 0.9935 | 0.2941 | 0.6987 |
| Initial Weight Combination Result | 0.4586 | 0.4369 | 0.9875 | 0.4117 | 0.6153 |
| User Guided Result | 0.6330 | 0.6284 | 0.9787 | 0.7997 | 0.5232 |

Individual learner results are shown in Table 3.7. The values in Table 3.7 are the average classification results of 19 CD13 images. Initial weight combination results indicate the first combined outcome with the initial weights. The User Guided Result row in Table 3.7 shows the results of the updated system after the user feedback.

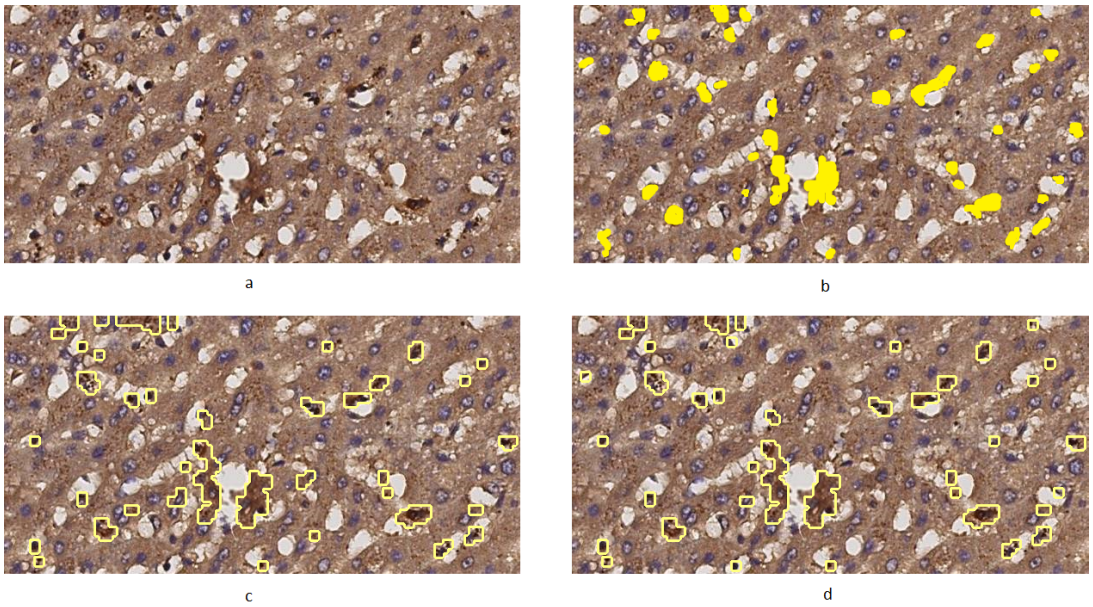


Figure 3.6: A CD13 stained image (a), its ground truth image marked by a pathologist (b), first result of the MoL algorithm (c), the image obtained after user feedbacks.

An output of the proposed algorithm is demonstrated in Figure 3.6. A CD13 image given in Figure 3.6 (a) is fed to the learning algorithm. The ground truth labels are shown in Figure 3.6 (b). The output obtained with the initial weights is shown in Figure 3.6 (c). The misdetected regions can be observed in 3.6 (c). In Figure 3.6 (d), the result obtained from the updated system with the user feedbacks is presented. It is evident from the figure that the number of misdetected regions are decreased.

In addition to the comparison of the MoL algorithm with the individual region descriptors, the MoL algorithm is compared with the Color Segmentation plug-in of ImageJ (`http://bigwww.epfl.ch/sage/soft/colorsegmentation/`) [57]. This plug-in allows user to select the desired regions for segmentation process. User can select up to 10 clusters and two different segmentation methods. These methods are the K-Means and Hidden Markov Models (HMM) clustering algorithms. However, for each image, the region selection process must be made

individually and it is not possible to undo the last selection. Since, HMM method adds spatial constraints into account, experiments are conducted with HMM and both independent and joint color data organizations are used.

Table 3.8: MoL vs ImageJ color segmentation plug-in.

| Image # | Mixture of Learners | | | Hidden Markov M. Ind. Color | | | Hidden Markov M. Joint Color | | |
|---|---|---|---|---|---|---|---|---|---|
| | MCC | F1 Score | Specificity | MCC | F1 Score | Specificity | MCC | F1 Score | Specificity |
| CD13-1 | 0.61 | 0.64 | 0.95 | 0.35 | 0.33 | 0.99 | 0.35 | 0.33 | 0.99 |
| CD13-2 | 0.61 | 0.61 | 0.96 | 0.40 | 0.47 | 0.97 | 0.40 | 0.47 | 0.97 |
| CD13-3 | 0.68 | 0.68 | 0.96 | 0.45 | 0.45 | 0.97 | 0.45 | 0.45 | 0.98 |
| CD13-4 | 0.63 | 0.62 | 0.96 | 0.43 | 0.45 | 0.97 | 0.48 | 0.47 | 0.99 |
| CD13-5 | 0.60 | 0.61 | 0.95 | 0.46 | 0.46 | 0.98 | 0.48 | 0.49 | 0.99 |
| CD13-6 | 0.63 | 0.63 | 0.95 | 0.46 | 0.48 | 0.97 | 0.47 | 0.48 | 0.98 |
| CD13-7 | 0.58 | 0.56 | 0.95 | 0.48 | 0.49 | 0.97 | 0.47 | 0.48 | 0.98 |
| CD13-8 | 0.53 | 0.52 | 0.98 | 0.37 | 0.38 | 0.99 | 0.40 | 0.39 | 0.99 |
| CD13-9 | 0.58 | 0.58 | 0.99 | 0.44 | 0.45 | 0.99 | 0.42 | 0.41 | 0.98 |
| CD13-10 | 0.65 | 0.65 | 0.99 | 0.43 | 0.43 | 0.98 | 0.42 | 0.43 | 0.98 |
| CD13-11 | 0.63 | 0.63 | 0.99 | 0.55 | 0.55 | 0.99 | 0.44 | 0.44 | 0.99 |
| CD13-12 | 0.70 | 0.69 | 0.99 | 0.48 | 0.49 | 0.99 | 0.45 | 0.44 | 0.98 |
| CD13-13 | 0.63 | 0.61 | 0.98 | 0.46 | 0.45 | 0.98 | 0.49 | 0.46 | 0.99 |
| CD13-14 | 0.59 | 0.59 | 0.99 | 0.35 | 0.30 | 0.97 | 0.23 | 0.17 | 0.96 |
| CD13-15 | 0.60 | 0.60 | 0.99 | 0.27 | 0.20 | 0.99 | 0.41 | 0.39 | 0.98 |
| CD13-16 | 0.67 | 0.65 | 0.97 | 0.61 | 0.62 | 0.98 | 0.56 | 0.56 | 0.97 |
| CD13-17 | 0.68 | 0.67 | 0.98 | 0.42 | 0.42 | 0.98 | 0.28 | 0.24 | 0.94 |
| CD13-18 | 0.63 | 0.61 | 0.99 | 0.43 | 0.44 | 0.99 | 0.39 | 0.39 | 0.99 |

As it is shown in Table 3.8, the MoL algorithm achieves better classification results compared to the ImageJ Color Segmentation plug-in. However, it is not possible to train a classifier with the ImageJ Color Segmentation plug-in. Trainable Weka Segmentation (TWS) (`http://imagej.net/Trainable_Weka_Segmentation`) plug-in in Fiji [13] is used at this end. The aim of the TWS plug-in is to combine the machine learning power of Weka [58] with the Fiji [13]. It allows user to select different feature extraction methods with many machine learning algorithms. In TWS, sample regions are selected by the user and the features are extracted from these regions. Then, a classifier is trained and used in segmentation of similar images. The user guided results of the MoL algorithm are compared with the TWS plug-in results. In TWS, mean and derivative values of the related regions (CSC and other regions.) are extracted as features and the

Fast-Random Forest method is used for classification. The Fast-Random Forest is the default classifier of the TWS and it is initialized with 200 trees and 2 random features per node. Detailed information about the TWS plug-in can be found at: (`http://imagej.net/Trainable_Weka_Segmentation`).

Table 3.9: MoL vs Trainable Weka Segmentation (TWS).

| Image # | Mixture of Learners | | TWS Fast-Random Forest | |
|---|---|---|---|---|
| | MCC | F1 Score | MCC | F1 Score |
| CD13-1 | 0.61 | 0.64 | 0.36 | 0.36 |
| CD13-2 | 0.61 | 0.61 | 0.42 | 0.44 |
| CD13-3 | 0.68 | 0.68 | 0.46 | 0.48 |
| CD13-4 | 0.63 | 0.62 | 0.46 | 0.48 |
| CD13-5 | 0.60 | 0.61 | 0.48 | 0.49 |
| CD13-6 | 0.63 | 0.63 | 0.46 | 0.47 |
| CD13-7 | 0.58 | 0.56 | 0.47 | 0.49 |
| CD13-8 | 0.53 | 0.52 | 0.38 | 0.38 |
| CD13-9 | 0.58 | 0.58 | 0.25 | 0.19 |
| CD13-10 | 0.65 | 0.65 | 0.22 | 0.18 |
| CD13-11 | 0.63 | 0.63 | 0.55 | 0.56 |
| CD13-12 | 0.70 | 0.69 | 0.56 | 0.56 |
| CD13-13 | 0.63 | 0.61 | 0.60 | 0.61 |
| CD13-14 | 0.59 | 0.59 | 0.54 | 0.54 |
| CD13-15 | 0.60 | 0.60 | 0.63 | 0.64 |
| CD13-16 | 0.67 | 0.65 | 0.63 | 0.42 |
| CD13-17 | 0.68 | 0.67 | 0.60 | 0.61 |
| CD13-18 | 0.63 | 0.61 | 0.17 | 0.12 |

In Table 3.9 MCC and F1 scores of the MoL algorithm and the TWS plug-in are shown. MCC and F1 are defined in Chapter 2. As it can be observed from the Table 3.9 that in some cases when the TWS plug-in is used very poor classification scores are achieved. It is because of the reason that, in TWS plug-in classifiers are trained with only one image. Thus, the trained classifier fails to classify an image which has different background color. However, the MoL algorithm is more robust to such changes and gives much better segmentation results than TWS.

## 3.3 Classification of H&E Images by Using 1-D SIFT Method

H&E stain is a cost effective routine histopathological technique [59–63]. Unlike CD13 images, it is difficult to distinguish CSCs in H&E images. CSCs appear in dark brown colors and can be easily noticed in a CD13 stained image. Thus, a method which can classify H&E images according to CSC densities would make this process cheaper and more accessible. The aim of this section is to present an algorithm to classify H&E images according to their CSC densities.

Before presenting the algorithm, it is necessary to briefly explain the relative parts of acquisition of these microscopic images from the patients. First, a sample tissue is taken from the patient and it is finely sliced in very thin layers (tissue sections). The adjacent sections look very similar but actually they are not exactly the same layer. Subsequently, the sections are stained with either H&E or CD13 stain. Note that an already stained section cannot be stained again with another dye/marker. For that reason, it is not possible to have both CD13 and H&E stained images of exactly the same tissue section. To overcome this problem, adjacent sections of the same tissue are stained with different stains assuming that they have similar cancer properties. Based on this assumption, CSC density calculated on a CD13 stained section image is associated with its adjacent layer which is stained with H&E. Therefore, ground truth information for H&E images is created.

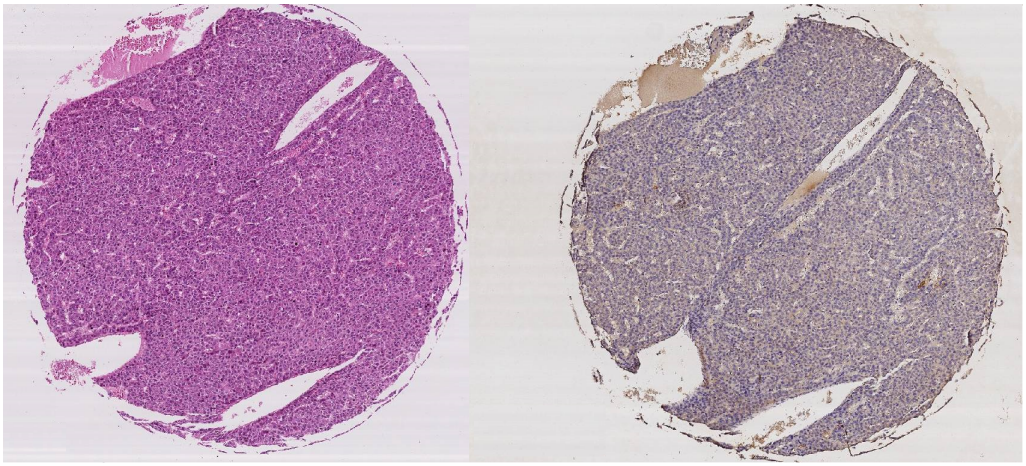

Figure 3.7: CD13 (left) and H&E (right) stained serial section tissue images of the same patient.

In Figure 3.7, the adjacent sections for the same tissue are shown. Various collocating regions of these images are chosen. CSC densities in the chosen regions are calculated as a percentage of CSCs to all cells. This process is carried out on the chosen image region of CD13 stained tissue. The calculated density also gives that of corresponding H&E regions. The ratio which gives us the CSC density in the chosen region is as follows:

$$CellRatio = \frac{\sum CSC}{\sum AllCells} \times 100 \quad . \tag{3.19}$$

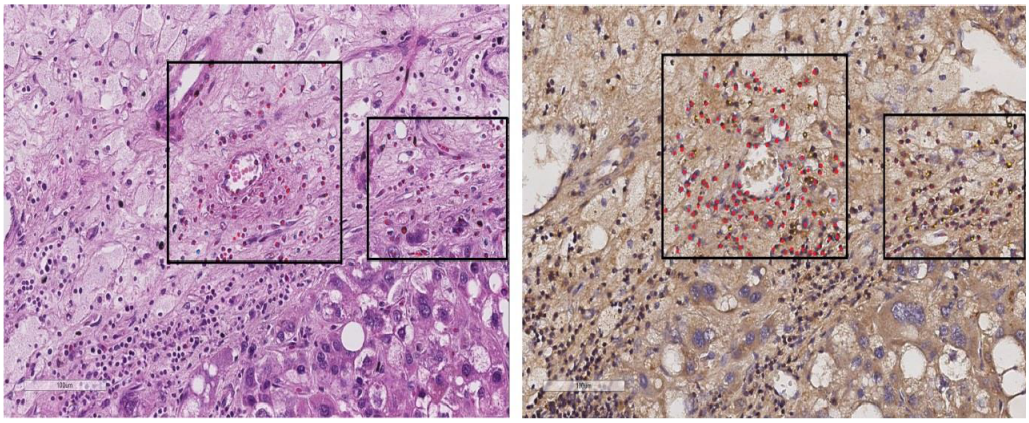

Figure 3.8: Corresponding regions of H&E (left) and CD13 (right) stained tissue images.

According to this ratio, a grading scheme is defined. If the Cell Ratio is less than 5%, that region is considered to have a low-grade and labeled as Grade-I. If it is greater or equal to 5%, it is labeled as a Grade-II meaning that it is a high-grade cancer region. It is noteworthy to remember that CD13 images are only used for labeling H&E images. They are not involved in the training stage in any way.

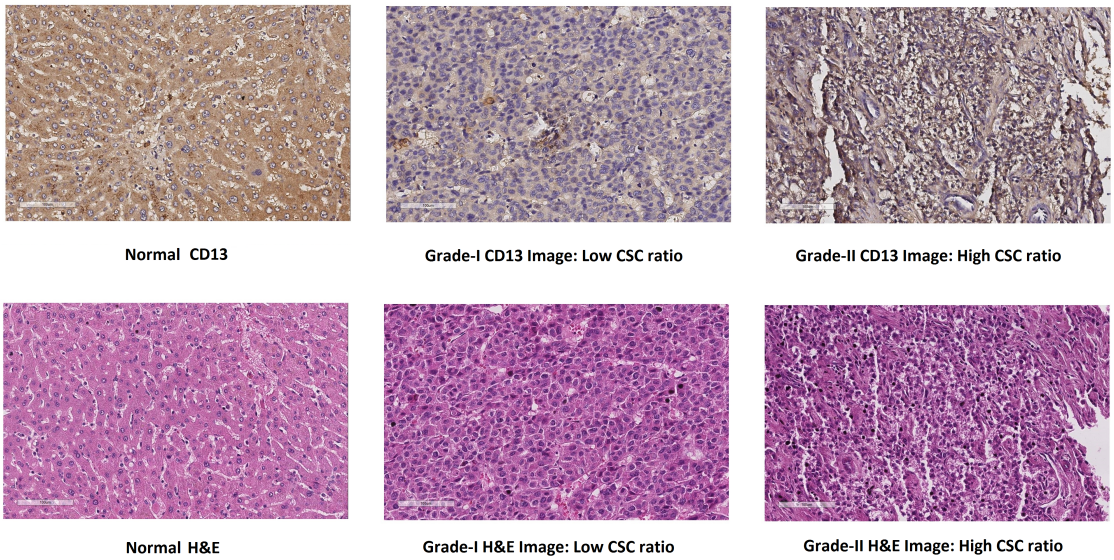


Figure 3.9: CD13 and H&E image examples according to estimated CSC levels.

In Figure 3.9 example images for normal, Grade-I and Grade-II are shown. These H&E images are fed into the 1-D SIFT algorithm, which is explained in the following Section 3.3.1.

### 3.3.1 1-D SIFT Algorithm

In [64] , 1-D SIFT algorithm is presented. It is inspired from famous the SIFT [22] algorithm and utilized in merging super pixels. However, steps like key point detection, feature vector extraction and matching are disregarded. In this work, 1-D SIFT algorithm is expanded to incorporate these steps and applied to an image classification problem.

In SIFT [22] , identical key points are extracted from 2-D images. The 1-D SIFT algorithm extracts the key points from the images color histograms. As in the 2-D SIFT method, 1-D histograms are filtered with 1-D difference of Gaussian

filters. Then, local extrema and minima locations are determined. Footprints of these extrema and minima points are backtracked from the lowest scale to the highest scale. If it is possible to backtrack an extrema or a minima location from coarsest level to the highest level, that location is taken as a key point. After the key point indexes are found, the gradient of the color histogram is calculated. Eight neighboring gradient values around the key points are taken. According to their magnitudes, they are placed into a feature vector.

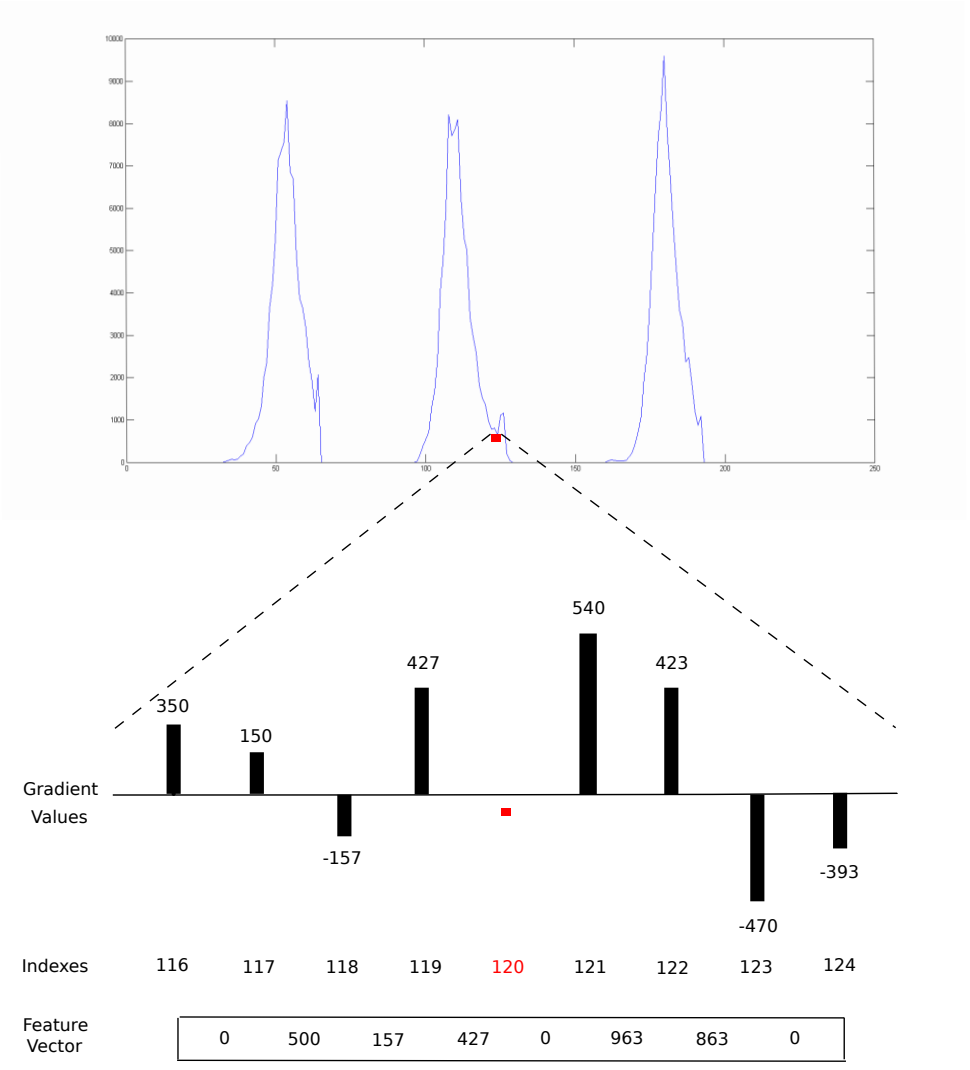


Figure 3.10: Feature vector extraction process in 1-D SIFT algorithm.

In Figure 3.10, the feature vector extraction process for the 1-D SIFT algorithm is graphically explained. A key point location is shown with a red dot on the 32-binned RGB histogram at index 120. Gradient values are paired together and according to their signs and their magnitudes placed into feature vector. The negative values are summed and inserted into the first element where positive ones are also summed and placed into the second element of the feature vector. Thus, a feature vector with four pairs is constructed. This process is applied to the all images in our data set.

### 3.3.2 Experimental Results

Serial sections of the same TMA samples stained with CD13 were deparaffinized and stained with Hematoxylin (Harris Hematoxylin)/Eosin-phloxine according to manufacturers protocol (Harris). H&E stained TMA samples are analyzed under a light microscope (EUROMEX-Oxion) and images are acquired with 20X objectives. Our image data set contains 454 H&E stained liver images which were taken from 56 different patients. 184 of these samples are from healthy patients and the other 270 images are taken from patients diagnosed with cancer. According to our grading ratio defined in Equation 3.19, 119 out of 270 are labeled as Grade-I and the tile size of the images are chosen as 300x300 pixels.

Several experiments are conducted in order to find the best way for the classification process. Since we do not have only one image for each patient, in each experiment, we follow "The Leave One Person Out" approach. First, we focus on differentiating normal images from cancerous images.

In our first experiment, Principal Component Analysis (PCA) is applied to the extracted feature vectors. The first eigenvectors are taken and fed into k-NN algorithm. The number of neighbors $k$ is taken as three. As a second experiment, the weighted combination of the first four eigenvectors and their linear combinations are computed. Best classification accuracy is obtained when five times of the first eigenvector is combined with the third eigenvector itself. Lastly, matching algorithms presented in Section 7.1 and 7.2 [65] of SIFT [22] are carried out.

In section 7.1 of [22], for each key point, a ratio between the distances of the first and second closest key point matches is calculated. The key points with ratios larger than 0.8 are disregarded. In section 7.2 of [22] the Best Bin First (BBF) algorithm is used for key point matching. An image classification is concluded after applying a majority voting decision rule on key point matches.

Table 3.10: Cancer vs normal image classification accuracies of conducted experiments.

| Experiment | Unnormalized (%) | Normalized (%) |
|---|---|---|
| PCA | 79.30 | 77.53 |
| PCA Linear Combination | 78.63 | 81.50 |
| Keypoint Matching (Section 7.1) | 86.50 | 82.81 |
| Efficient Nearest Neighbor Indexing | 86.56 | 82.81 |

In Table 3.10, classification accuracies of conducted experiments are presented. In the normalized case, feature vector entities are normalized by dividing each element $L_2$ norm of the feature vector. These experiments are carried out on feature vectors extracted from RGB histogram. To observe the effect of the different color spaces in our classification problem, similar experiments are applied for both HSV and YCbCr color histograms. To be consistent with the SIFT algorithm [22] , only the Keypoint Matching and the Efficient Nearest Neighbor Indexing (BBF) experiments are taken into consideration.

Table 3.11: Cancer vs normal image classification accuracies of conducted experiments in different color spaces with unnormalized feature vectors.

| Experiment (Unnormalized) | HSV (%) | YCbCr (%) | RGB (%) |
|---|---|---|---|
| Keypoint Matching | 88.54 | 89.86 | 86.50 |
| Efficient Nearest Neighbor Indexing | 88.54 | 89.86 | 86.50 |

Table 3.12: Cancer vs normal image classification accuracies of conducted experiments in different color spaces with normalized feature vectors.

| Experiment (Normalized) | HSV (%) | YCbCr (%) | RGB (%) |
|---|---|---|---|
| Keypoint Matching | 85.02 | 81.27 | 82.81 |
| Efficient Nearest Neighbor Indexing | 85.02 | 81.27 | 82.81 |

As it can be seen from Tables 3.11 and 3.12, in the feature vector extraction stage, using different color space histograms has a positive effect on classification results. Also, applying normalization on the extracted feature vectors affects the accuracies of the classification results negatively. Experiments are expanded by combining different color channels. Since YCbCr color domain gives the best classification results so far, channels of HSV and RGB color domains are combined with the YCbCr color histogram.

Table 3.13: Constructed combinations with different color domains. Experiments are conducted with keypoint matching algorithm.

| Combination | Unnormalized (%) | Normalized (%) |
|---|---|---|
| YCbCr+H | 89.42 | 81.27 |
| YCbCr+S | 90.08 | 79.73 |
| YCbCr+V | 90.52 | 81.27 |
| YCbCr+V+R | 89.20 | 78.41 |
| YCbCr+V+G | 90.96 | 80.39 |
| YCbCr+V+G+S | 89.86 | 79.95 |
| YCbCr+V+G+H | 87.44 | 79.07 |
| YCbCr+V+G+B | 90.74 | 80.39 |
| YCbCr+HSV+RGB | 89.42 | 80.39 |

Table 3.14: Constructed combinations with different color domains. Experiments are conducted with efficient nearest neighbor indexing (BBF) method.

| Combination | Unnormalized (%) | Normalized (%) |
|---|---|---|
| YCbCr+H | 89.42 | 81.27 |
| YCbCr+S | 90.30 | 79.51 |
| YCbCr+V | 90.74 | 81.05 |
| YCbCr+V+R | 89.20 | 78.63 |
| YCbCr+V+G | 90.96 | 80.83 |
| YCbCr+V+G+S | 90.08 | 80.17 |
| YCbCr+V+G+H | 87.44 | 79.07 |
| YCbCr+V+G+B | 90.74 | 80.61 |
| YCbCr+HSV+RGB | 89.42 | 80.39 |

As it is shown in Tables 3.13 and 3.14, using the YCbCr+V+G color histogram combination gives the best classification accuracy in the classification of normal and cancerous images.

Table 3.15: Confusion matrix of YCbCr+V+G.

| Class | Normal | Cancerous |
|---|---|---|
| Normal | 147 | 37 |
| Cancerous | 4 | 266 |

Table 3.16: Grade-I vs Grade-II: Confusion matrix of YCbCr+V+G.

| Class | Grade-I | Grade-II |
|---|---|---|
| Grade-I | 20 | 99 |
| Grade-II | 34 | 117 |

Table 3.17: Confusion matrix of YCbCr+V+G case in three class classification problem.

| Class | Normal | Grade-I | Grade-II |
|---|---|---|---|
| Normal | 173 | 2 | 9 |
| Grade-I | 17 | 20 | 82 |
| Grade-II | 27 | 27 | 97 |

In Table 3.15, the confusion matrix of the YCbCr+V+G case is given. Since the best classification result is achieved with YCbCr+V+G combination, in the classification of Grade-I and Grade-II images the same combination is used. However, with the chosen color histogram combination we achieve 51% classification accuracy. In Tables 3.16 and 3.17, confusion matrices of the related problem are shown. Although it can distinguish normal from cancerous tissue images, the 1-D SIFT algorithm fails to differentiate between Grade-I and Grade-II images.

In addition to experiments carried out with the unnormalized YCbCr case, experiments with the normalized HSV color histograms are also conducted. As it can be seen from the Table 3.12, HSV color space has the highest score in normalized case. Thus, the same matching algorithms are applied to the HSV color histogram combined with the YCbCr and the RGB channels.

Table 3.18: Constructed HSV histogram combinations with different color domains.

| Combination | Keypoint Matching (%) | BBF (%) |
|---|---|---|
| HSV+R | 82.59 | 82.59 |
| HSV+G | 85.46 | 85.46 |
| HSV+B | 83.03 | 83.03 |
| HSV+Y | 83.70 | 83.70 |
| HSV+Cb | 83.03 | 83.03 |
| HSV+Cr | 86.56 | 86.56 |
| HSV+G+Cb | 83.03 | 83.03 |
| HSV+G+Y | 84.58 | 84.58 |
| HSV+G+R | 83.70 | 83.70 |
| HSV+G+B | 83.48 | 83.48 |
| HSV+Cr+G | 85.24 | 85.24 |
| HSV+Cr+B | 83.03 | 83.03 |
| HSV+Cr+R | 85.02 | 85.02 |

Table 3.19: Confusion matrix of HSV+Cr case in three class classification problem.

| Class | Normal | Grade-I | Grade-II |
|---|---|---|---|
| Normal | 160 | 7 | 17 |
| Grade-I | 24 | 20 | 75 |
| Grade-II | 33 | 43 | 75 |

In Table 3.18, the best classification result is achieved when HSV color histogram is combined with Cr channel. However, as it is shown in In Table 3.19, when the same color histogram combination is used for the classification of Grade-I and Grade-II images, the algorithm fails.

# Chapter 4

# Conclusion

In this thesis, a variety of algorithms for stem cell detection, segmentation and classification of the cancerous images are presented. With the implemented algorithms, this thesis aims to help pathologists in their tedious work.

In Chapter 2, a new multi-resolution super-pixel method is proposed. The purpose is to represent a Mesenchymal Stem Cell (MSC) using a couple of super-pixels because super-pixels give reliable segmentation results. Initial seed locations of the multi-resolution super-pixels are determined according to local wavelet energy of the image rather than Simple Linear Iterative Clustering method (SLIC). It is experimentally shown that when the implemented algorithm was used instead of the SLIC algorithm, the cell detection rate increased by 7% and the false alarm rate in the same stage decreased by 5%. In addition to the multi-resolution super-pixel algorithm, two super-pixel merging algorithms are presented. The first algorithm was a 1-D version of the well-known SIFT algorithm which is designed for matching 2-D image regions. The proposed 1-D SIFT algorithm is the first approach in the literature which takes advantage of SIFT in one dimension. 1-D SIFT features are the indexes, which are the extrema of the Difference of Gaussians (DoG) occurring at multiple resolution scales of color histograms. When the indexes of color histograms match, the corresponding regions are identified as similar regions and merged. Thus, more apparent representation

of stem cells is achieved. It is also shown that super-pixel regions can be merged with the use of wavelets. It is experimentally observed that, both merging methods are able to achieve high MCC and F1 scores. Although, both methods have very close results, the wavelet merging algorithm gives better performance. With these merging algorithms, it is possible to determine the background and identify cell nuclei as well as cytoplasm in MSCs images without using any threshold.

In Chapter 3, it is shown that the region co-difference and the region covariance methods can be used for cancer stem cell detection in CD13 stained tissue images. Although these two methods are used in many other applications, they have not been employed for detection of cancer stem cells in such images. These methods are compared using both F1 score and MCC. From both comparison methods we can conclude that although the covariance method has close scores, the co-difference method gives better F1 and Matthews Correlation Coefficient (MCC) scores in 13 out of 18 images. In Section 3.2, a CAD module with an online decision fusion strategy is presented. Prediction results of the several region descriptors are linearly combined and the predicted image shown to the user via GUI. It is experimentally shown that instead of using region descriptors individually, using the proposed approach leads to an approximate 25% increase in both F1 and MCC scores. Also, the proposed module is compared with the similar plug-ins of ImageJ and Fiji. It is shown that, when the similar features are used, the implemented module achieves approximately 20% better classification results compared to the plug-ins of Imagej and Fiji. Moreover, the aforementioned 1-D SIFT algorithm is expanded and it is experimentally shown that the expanded 1-D SIFT algorithm is able to classify healthy and cancerous tissues with up to 91% accuracy in H&E stained images. Although it is able to classify normal and cancerous tissues with a high accuracy, the algorithm fails to differentiate between Grade-I and Grade-II cancerous images. The reason might be that he feature parameters used in this thesis are not fine enough to find the faint differences. However, it is possible to classify them with 75% accuracy using different approaches [66].

# Bibliography


[1] B. Stewart, C. P. Wild, *et al.*, "World cancer report 2014," *World*, 2015.

[2] J. Monaco, J. Tomaszewski, M. Feldman, M. Moradi, P. Mousavi, A. Boag, C. Davidson, P. Abolmaesumi, and A. Madabhushi, "Detection of prostate cancer from whole-mount histology images using markov random fields," in *Workshop on Microscopic Image Analysis with Applications in Biology (in conjunction with MICCAI)*, 2008.

[3] A. Basavanhally, S. Agner, G. Alexe, G. Bhanot, S. Ganesan, and A. Madabhushi, "Manifold learning with graph-based features for identifying extent of lymphocytic infiltration from high grade, her2+ breast cancer histology," *Image Anal. Appl. Biol.(in Conjunction MICCAI), New York [Online]. Available: http://www. miaab. org/miaab-2008-papers/27-miaab-2008-paper-21. pdf*, 2008.

[4] F. Aurenhammer, "Voronoi diagramsa survey of a fundamental geometric data structure," *ACM Computing Surveys (CSUR)*, vol. 23, no. 3, pp. 345–405, 1991.

[5] T. Kiang, "Random fragmentation in two and three dimensions," *Zeitschrift fur Astrophysik*, vol. 64, p. 433, 1966.

[6] R. L. Graham and P. Hell, "On the history of the minimum spanning tree problem," *Annals of the History of Computing*, vol. 7, no. 1, pp. 43–57, 1985.

[7] M. N. Gurcan, L. E. Boucheron, A. Can, A. Madabhushi, N. M. Rajpoot, and B. Yener, "Histopathological image analysis: a review," *Biomedical Engineering, IEEE Reviews in*, vol. 2, pp. 147–171, 2009.

[8] J. W. Lichtman and J.-A. Conchello, "Fluorescence microscopy," *Nature methods*, vol. 2, no. 12, pp. 910–919, 2005.

[9] G. W. Gordon, G. Berry, X. H. Liang, B. Levine, and B. Herman, "Quantitative fluorescence resonance energy transfer measurements using fluorescence microscopy," *Biophysical journal*, vol. 74, no. 5, pp. 2702–2713, 1998.

[10] E. M. Goldys, *Fluorescence applications in biotechnology and life sciences*. John Wiley & Sons, 2009.

[11] L. He, L. R. Long, S. Antani, and G. R. Thoma, "Histology image analysis for carcinoma detection and grading," *Computer methods and programs in biomedicine*, vol. 107, no. 3, pp. 538–556, 2012.

[12] M. D. Abràmoff, P. J. Magalhães, and S. J. Ram, "Image processing with imagej," *Biophotonics international*, vol. 11, no. 7, pp. 36–42, 2004.

[13] J. Schindelin, I. Arganda-Carreras, E. Frise, V. Kaynig, M. Longair, T. Pietzsch, S. Preibisch, C. Rueden, S. Saalfeld, B. Schmid, *et al.*, "Fiji: an open-source platform for biological-image analysis," *Nature methods*, vol. 9, no. 7, pp. 676–682, 2012.

[14] A. E. Carpenter, T. R. Jones, M. R. Lamprecht, C. Clarke, I. H. Kang, O. Friman, D. A. Guertin, J. H. Chang, R. A. Lindquist, J. Moffat, *et al.*, "Cellprofiler: image analysis software for identifying and quantifying cell phenotypes," *Genome biology*, vol. 7, no. 10, p. R100, 2006.

[15] J. R. Swedlow, I. Goldberg, E. Brauner, and P. K. Sorger, "Informatics and quantitative analysis in biological imaging," *Science*, vol. 300, no. 5616, pp. 100–102, 2003.

[16] I. G. Goldberg, C. Allan, J.-M. Burel, D. Creager, A. Falconi, H. Hochheiser, J. Johnston, J. Mellen, P. K. Sorger, and J. R. Swedlow, "The open microscopy environment (ome) data model and xml file: open tools for informatics and quantitative analysis in biological imaging," *Genome biology*, vol. 6, no. 5, p. R47, 2005.

[17] C. Allan, J.-M. Burel, J. Moore, C. Blackburn, M. Linkert, S. Loynton, D. MacDonald, W. J. Moore, C. Neves, A. Patterson, *et al.*, "Omero: flexible, model-driven data management for experimental biology," *Nature methods*, vol. 9, no. 3, pp. 245–253, 2012.

[18] N. Orlov, L. Shamir, T. Macura, J. Johnston, D. M. Eckley, and I. G. Goldberg, "Wnd-charm: Multi-purpose image classification using compound image transforms," *Pattern recognition letters*, vol. 29, no. 11, pp. 1684–1693, 2008.

[19] H. Peng, Z. Ruan, F. Long, J. H. Simpson, and E. W. Myers, "V3d enables real-time 3d visualization and quantitative analysis of large-scale biological image data sets," *Nature biotechnology*, vol. 28, no. 4, pp. 348–353, 2010.

[20] M. R. Berthold, N. Cebron, F. Dill, T. R. Gabriel, T. Kötter, T. Meinl, P. Ohl, C. Sieb, K. Thiel, and B. Wiswedel, "Knime: The konstanz information miner," in *Data analysis, machine learning and applications*, pp. 319–326, Springer, 2008.

[21] F. De Chaumont, S. Dallongeville, and J.-C. Olivo-Marin, "Icy: A new open-source community image processing software," in *Biomedical Imaging: From Nano to Macro, 2011 IEEE International Symposium On*, pp. 234–237, IEEE, 2011.

[22] D. G. Lowe, "Distinctive image features from scale-invariant keypoints," *International journal of computer vision*, vol. 60, no. 2, pp. 91–110, 2004.

[23] O. Tuzel, F. Porikli, and P. Meer, "Region covariance: A fast descriptor for detection and classification," in *Computer Vision–ECCV 2006*, pp. 589–600, Springer, 2006.

[24] H. Tuna, I. Onaran, *et al.*, "Image description using a multiplier-less operator," *Signal Processing Letters, IEEE*, vol. 16, no. 9, pp. 751–753, 2009.

[25] O. Oguz, C. Muenzenmayer, T. Wittenberg, A. Uner, A. E. Cetin, and R. C. Atalay, "Detection of cancer stem cells in microscopic images by using region covariance and codifference method," in *Computational Intelligence*

*for Multimedia Understanding (IWCIM), 2015 International Workshop on*, pp. 1–5, IEEE, 2015.

[26] S. Yarkan, B. U. Töreyin, K. Qaraqe, *et al.*, "An online adaptive cooperation scheme for spectrum sensing based on a second-order statistical method," *Vehicular Technology, IEEE Transactions on*, vol. 61, no. 2, pp. 675–686, 2012.

[27] O. Günay, B. U. Töreyin, and A. E. Cetin, "Online adaptive decision fusion framework based on projections onto convex sets with application to wildfire detection in video," *Optical Engineering*, vol. 50, no. 7, pp. 077202–077202, 2011.

[28] S. Wang, H. Lu, F. Yang, and M.-H. Yang, "Superpixel tracking," in *Computer Vision (ICCV), 2011 IEEE International Conference on*, pp. 1323–1330, IEEE, 2011.

[29] G. Mori, "Guiding model search using segmentation," in *Computer Vision, 2005. ICCV 2005. Tenth IEEE International Conference on*, vol. 2, pp. 1417–1423, IEEE, 2005.

[30] B. Micusik and J. Kosecka, "Semantic segmentation of street scenes by superpixel co-occurrence and 3d geometry," in *Computer Vision Workshops (ICCV Workshops), 2009 IEEE 12th International Conference on*, pp. 625–632, IEEE, 2009.

[31] R. Achanta, A. Shaji, K. Smith, A. Lucchi, P. Fua, and S. Susstrunk, "Slic superpixels compared to state-of-the-art superpixel methods," *Pattern Analysis and Machine Intelligence, IEEE Transactions on*, vol. 34, no. 11, pp. 2274–2282, 2012.

[32] D. G. Lowe, "Object recognition from local scale-invariant features," in *Computer vision, 1999. The proceedings of the seventh IEEE international conference on*, vol. 2, pp. 1150–1157, Ieee, 1999.

[33] C. Liu, J. Yuen, and A. Torralba, "Sift flow: Dense correspondence across scenes and its applications," *Pattern Analysis and Machine Intelligence, IEEE Transactions on*, vol. 33, no. 5, pp. 978–994, 2011.

[34] P. Scovanner, S. Ali, and M. Shah, "A 3-dimensional sift descriptor and its application to action recognition," in *Proceedings of the 15th international conference on Multimedia*, pp. 357–360, ACM, 2007.

[35] S. Haas, R. Donner, A. Burner, M. Holzer, and G. Langs, "Superpixel-based interest points for effective bags of visual words medical image retrieval," in *Medical Content-Based Retrieval for Clinical Decision Support*, pp. 58–68, Springer, 2012.

[36] F. Navarro, M. Escudero-Viñolo, and J. Bescós, "Sp-sift: enhancing sift discrimination via super-pixel-based foreground–background segregation," *Electronics Letters*, vol. 50, no. 4, pp. 272–274, 2014.

[37] A. E. Cetin and R. Ansari, "Signal recovery from wavelet transform maxima," *IEEE Transactions on Signal Processing*, vol. 42, no. 1, pp. 194–196, 1994.

[38] S. G. Mallat, "A theory for multiresolution signal decomposition: the wavelet representation," *Pattern Analysis and Machine Intelligence, IEEE Transactions on*, vol. 11, no. 7, pp. 674–693, 1989.

[39] J. M. Shapiro, "Embedded image coding using zerotrees of wavelet coefficients," *IEEE Transactions on Signal Processing*, vol. 41, no. 12, pp. 3445–3462, 1993.

[40] S. G. Chang, B. Yu, and M. Vetterli, "Adaptive wavelet thresholding for image denoising and compression," *IEEE Transactions on Image Processing*, vol. 9, no. 9, pp. 1532–1546, 2000.

[41] A. E. Cetin and M. Tofighi, "Projection-based wavelet denoising," *IEEE Signal Processing Magazine*, vol. 32, no. 5, pp. 120–124, 2015.

[42] A. Yazar, F. Keskin, B. U. Töreyin, and A. E. Çetin, "Fall detection using single-tree complex wavelet transform," *Pattern Recognition Letters*, vol. 34, no. 15, pp. 1945–1952, 2013.

[43] A. M. Wink and J. B. Roerdink, "Denoising functional mr images: a comparison of wavelet denoising and gaussian smoothing," *Medical Imaging, IEEE Transactions on*, vol. 23, no. 3, pp. 374–387, 2004.

[44] B. W. Matthews, "Comparison of the predicted and observed secondary structure of t4 phage lysozyme," *Biochimica et Biophysica Acta (BBA)-Protein Structure*, vol. 405, no. 2, pp. 442–451, 1975.

[45] Y. Yang and X. Liu, "A re-examination of text categorization methods," in *Proceedings of the 22nd annual international ACM SIGIR conference on Research and development in information retrieval*, pp. 42–49, ACM, 1999.

[46] F. Porikli, O. Tuzel, and P. Meer, "Covariance tracking using model update based on lie algebra," in *Computer Vision and Pattern Recognition, 2006 IEEE Computer Society Conference on*, vol. 1, pp. 728–735, IEEE, 2006.

[47] H. Murase and S. K. Nayar, "Visual learning and recognition of 3-d objects from appearance," *International journal of computer vision*, vol. 14, no. 1, pp. 5–24, 1995.

[48] S. L. Phung, A. Bouzerdoum, and D. Chai, "A novel skin color model in ycbcr color space and its application to human face detection," in *Image Processing. 2002. Proceedings. 2002 International Conference on*, vol. 1, pp. I–289, IEEE, 2002.

[49] Š. Obdržálek and J. Matas, "Local affine frames for image retrieval," in *Image and Video Retrieval*, pp. 318–327, Springer, 2002.

[50] D.-M. Tsai, H.-T. Hou, and H.-J. Su, "Boundary-based corner detection using eigenvalues of covariance matrices," *Pattern Recognition Letters*, vol. 20, no. 1, pp. 31–40, 1999.

[51] K. Duman, A. Eryildirim, and A. E. Cetin, "Target detection and classification in sar images using region covariance and co-difference," in *SPIE Defense, Security, and Sensing*, pp. 73370P–73370P, International Society for Optics and Photonics, 2009.

[52] K. Duman and A. E. Çetin, "Target detection in sar images using codifference and directional filters," in *SPIE Defense, Security, and Sensing*, pp. 76990S–76990S, International Society for Optics and Photonics, 2010.

[53] F. Cogun and A. E. Çetin, "Object tracking under illumination variations using 2d-cepstrum characteristics of the target," in *Multimedia Signal Processing (MMSP), 2010 IEEE International Workshop on*, pp. 521–526, IEEE, 2010.

[54] V. N. Vapnik and V. Vapnik, *Statistical learning theory*, vol. 1. Wiley New York, 1998.

[55] C.-C. Chang and C.-J. Lin, "LIBSVM: A library for support vector machines," *ACM Transactions on Intelligent Systems and Technology*, vol. 2, pp. 27:1–27:27, 2011. Software available at `http://www.csie.ntu.edu.tw/~cjlin/libsvm`.

[56] K. Duman, "Methods for target detection in sar images," 2009.

[57] D. Sage, "Color segmentation: Imagej plugin to cluster color pixel driven by the user input," 2008. Software available at `http://bigwww.epfl.ch/sage/soft/colorsegmentation/`.

[58] M. Hall, E. Frank, G. Holmes, B. Pfahringer, P. Reutemann, and I. H. Witten, "The weka data mining software: an update," *ACM SIGKDD explorations newsletter*, vol. 11, no. 1, pp. 10–18, 2009.

[59] M. Veta, J. P. Pluim, P. J. van Diest, M. Viergever, *et al.*, "Breast cancer histopathology image analysis: A review," *Biomedical Engineering, IEEE Transactions on*, vol. 61, no. 5, pp. 1400–1411, 2014.

[60] E. Cosatto, M. Miller, H. P. Graf, and J. S. Meyer, "Grading nuclear pleomorphism on histological micrographs," in *Pattern Recognition, 2008. ICPR 2008. 19th International Conference on*, pp. 1–4, IEEE, 2008.

[61] R. Bhagavatula, M. Fickus, W. Kelly, C. Guo, J. Ozolek, C. Castro, J. Kovačevi, *et al.*, "Automatic identification and delineation of germ layer components in h&e stained images of teratomas derived from human and

nonhuman primate embryonic stem cells," in *Biomedical Imaging: From Nano to Macro, 2010 IEEE International Symposium on*, pp. 1041–1044, IEEE, 2010.

[62] S. Petushi, C. Katsinis, C. Coward, F. Garcia, and A. Tozeren, "Automated identification of microstructures on histology slides," in *Biomedical Imaging: Nano to Macro, 2004. IEEE International Symposium on*, pp. 424–427, IEEE, 2004.

[63] O. Sertel, G. Lozanski, A. Shana'ah, and M. N. Gurcan, "Computer-aided detection of centroblasts for follicular lymphoma grading using adaptive likelihood-based cell segmentation," *Biomedical Engineering, IEEE Transactions on*, vol. 57, no. 10, pp. 2613–2616, 2010.

[64] O. Yorulmaz, O. Oguz, E. Akhan, D. Tuncel, R. C. Atalay, and A. E. Cetin, "Multi-resolution super-pixels and their applications on fluorescent mesenchymal stem cells images using 1-d sift merging," in *Image Processing (ICIP), 2015 IEEE International Conference on*, pp. 2495–2499, IEEE, 2015.

[65] A. Vedaldi and B. Fulkerson, "VLFeat: An open and portable library of computer vision algorithms." `http://www.vlfeat.org/`, 2008.

[66] O. Oğuz, C. E. Akbaş, M. Mallah, K. Taşdemir, E. A. Güzelcan, C. Muenzenmayer, T. Wittenberg, A. Üner, A. Cetin, and R. Ç. Atalay, "Mixture of learners for cancer stem cell detection using cd13 and h and e stained images," in *SPIE Medical Imaging*, pp. 97910Y–97910Y, International Society for Optics and Photonics, 2016.